STOCHASTIC AND ANALYTICAL EXPLORATION OF ENHANCED GEOTHERMAL SYSTEM VIABILITY ON THE SNAKE RIVER PLAIN, IDAHO

A Thesis

Presented in Partial Fulfillment of the Requirements for the

Degree of Master of Science

with a

Major in Geological Sciences

in the

College of Graduate Studies

University of Idaho

by Alex C. Moody

December 2014

Major Professor: Jerry P. Fairley, Jr., Ph.D.

Authorization to Submit Thesis

This thesis of Alex Moody, submitted for the degree of Master of Science with a Major in Geological Sciences and titled "Stochastic and Analytical Exploration of Enhanced Geothermal System Viability on the Snake River Plain, Idaho," has been reviewed in final form. Permission, as indicated by the signatures and dates below, is now granted to submit final copies to the College of Graduate Studies for approval.

Major Professor:	_____	_____
	Jerry P. Fairley Jr., Ph.D.	Date
Committee Members:	_____	_____
	Brian Yanites, Ph.D.	Date
	_____	_____
	David Alexander, Ph.D.	Date
Department Administrator:	_____	_____
	Mickey Gunter, Ph.D.	Date
Dean, College of Science:	_____	_____
	Paul Joyce, Ph.D.	Date

Final Approval and Acceptance

Dean, College of Graduate Studies:	_____	_____
	Jie Chen, Ph.D.	Date

Abstract

Geothermal energy depends on high geothermal gradients, adequate permeability and accessible groundwater supply to support heat exchange with surrounding rock. Some regions may have an adequate heat resource but lack the necessary permeability or deep circulating water. Exploitation of such areas for geothermal energy could occur if permeability can be enhanced enough to provide the necessary heat exchange. This process would produce what is termed an 'enhanced geothermal system' (EGS).

The Snake River Plain in southern Idaho is a high heat flux (110 mW/m^2) region that has been recommended as an EGS target. We consider how the geologic and thermal history of the SRP might influence its EGS potential. We describe core recovered from one of the few deep boreholes located on the SRP. Fracture distribution data are then used to estimate cooling of water temperatures from a production well using a semi-analytical heat transfer model. Results delineate criteria for a hydraulic fracturing plan for augmenting the permeability and connectivity of the reservoir's preexisting fracture network.

Acknowledgements

I'd like thank John Shervais and the geology department at Utah State as well as Project HOTSPOT for access to their core laboratory and digital image database. Shea Newton helped with formatting my thesis into this visually appealing LaTeX document. Thanks to my band, the Terminal Morons, for cathartic noise making. This project was undergone as partial completion for a master's thesis and was funded by a Dept. of Energy LDRD in conjunction with the Idaho National Lab's Center for Advanced Energy Studies.

Table of Contents

List of Figures

List of Tables

Chapter 1: Introduction and Motivation

Geothermal energy is a prominent source of alternative energy used around the world that is helping to fulfill the need for emission-free power sources. It provided an estimated 67,000 GWh of energy in 2010 from ∼11,000 MW of installed power in suitable hydrogeologic settings across 24 countries (Bertani, 2012). Many of the high-temperature geothermal reservoirs being produced today are situated in young volcanic fields (the Taupo Volcanic Zone in New Zealand and many fields in Iceland, for example) (Donaldson, 1982). Such reservoirs typically are drilled into active hydrothermal systems that access hot fluids in a fractured matrix with energy replenishment via deep circulation. The necessary stored heat, at accessible depths, exists in many locations without natural hydrothermal circulation. The stored energy could be exploited if the permeability of the source rock can be sufficiently enhanced through hydraulic fracturing or other means, which is the driving concept behind an enhanced geothermal system (EGS).

In the western U.S., a proposed target for EGS development is the Snake River Plain (SRP) (Tester et al., 2006). The eastern SRP reflects relatively recent volcanic activity in the form of a series of collapsed calderas that destroyed the preexisting topography and left an extensive plain of coalesced lava flows. After cessation of the volcanic activity associated with caldera formation, large crustal magma bodies on the scale of the width of the postulated SRP calderas would maintain high temperature hydrothermal systems in the shallow subsurface for approximately 2 My (Kolstad and McGetchin, 1978). The ages of ignimbrites in the buried calderas of the SRP region indicate that the Bruneau-Jarbridge field and the Heise volcanic field were active at 12 Ma and 6.5-4.3 Ma, respectively. Thus, any residual heat and circulation in the associated hydrothermal systems would likely be depleted and mineralized. However, only an estimated 1%-10% of the total thermal energy provided by caldera eruption and collapse is in the hydrothermal system of the caldera. The remaining energy resides in low-permeability matrix and residual magma at depth (Wohletz and Heiken, 1992).

Accessing the heat stored in low-permeability zones, via development of an EGS could thus be the key to unlocking the geothermal potential of the relatively shallow subsurface in the SRP. The ability to accomplish that development is becoming more of a reality as EGS techniques are developed and tested as a means of increasing reservoir lifespan of conventional geothermal

systems. Injection of geothermal wastewater has become more common as a means of pressure support and as a way to increase extraction rates from a reservoir. Hydraulic fracturing methods have advanced dramatically in the last decade through rapid growth of shale oil and shale gas development and those techniques are currently being tested for EGS development at sites like Coso, Desert Peak, Glass Mountain, Newberry, Raft River, which are just examples from the United States (Tester et al., 2006). With increasing use and understanding of injection and the application of hydraulic fracturing for geothermal reservoir enhancement, areas like the SRP could provide the next generation of geothermal power resources. The SRP has heretofore been regarded as a high-potential EGS target primarily because of its high heat flux, one of the highest in North America (Blackwell and Richards, 2004). In this study, we seek to provide additional information necessary for evaluating the suitability of rhyolites that underlie the SRP and that are considered a target for EGS development.

We explore the feasibility of a commercial geothermal power plant on the SRP on the basis of core observations, which provide information about basic fracture geometries in the rhyolite, a parameter often not taken into account in reporting of in-place heat energy. To illustrate how the observed fractured distributions might affect geothermal energy recovery, we use semi-analytical solutions to heat transport in fractures.

1.1 Background

1.2 Geologic and thermal setting

The SRP, seen in figure 1.1, is a large volcanic province in the northwestern United States. Near Twin Falls, at $\sim$114° longitude, a distinction is made between the western and eastern Snake River Plain (WSRP, ESRP). Whereas the WSRP is a structural graben and measured heat flows are similar to the Basin and Range ($\sim$75 mW/m^2), there is minimal faulting along the margins of the ESRP and heat flows are elevated to $\sim$110 mW/m^2 (Blackwell et al., 2010; Shervais et al., 2013). Recent consensus contends that the ESRP formed as the North American Plate traveled southwest over a stationary mantle-plume hotspot (Leeman, 1982). Bimodal volcanism cut across the northern Basin and Range creating a large swath of volcanic fields 550 km by

100 km extending from the 16-Ma McDermitt field in southwestern Idaho and northeastern Nevada to the 2-Ma Yellowstone Plateau (Brott et al., 1981; Morgan and McIntosh, 2005). Nested caldera structures record time-transgressive younging to the ENE of ignimbrites and lavas created by hot, dry and voluminous silicic volcanism as the North American plate moved WSW at approximately 3 - 3.5 cm/yr (Branney et al., 2007; Shervais et al., 2005). Erupted volumes of lava estimated from individual tuff units range from 750 km^3 to 1800 km^3 with individual eruptions estimated at 0.5 km^3 (Morgan and McIntosh, 2005). The tuff deposits are capped by post-hotspot basalts that have been erupting up until 2 ka (Shervais et al., 2005). The hotspot concept for the formation of the SRP has a broad spectrum of supporting evidence including tectonic uplift and subsequent collapse along the track of the hotspot, a large geoid anomaly underneath Yellowstone, seismic tomography, and helium isotopes (Shervais et al., 2005).

Exposures of voluminous silicic volcanics largely reside along the margins of the SRP. Descriptions of and correlations between tuff units document the extreme heterogeneity in rheologic properties between separate flows (Morgan et al., 1984). Differences in volcanic features, such as vitrophyres and lithophysae, and long-term alteration processes, such as devitrification, will influence the hydrologic character of potential geothermal reservoirs on the ESRP (Fuller and Sharp, 1992).

1.3 Heat Flow

Heat flow through the crustal lithosphere from the influence of the hotspot has directly formed many of the modern topographic features on the ESRP. Thermal buoyancy effects can account for the 0.5 - 2 km of broad regional uplift caused by the migrating hotspot (Pierce and Morgan, 1992). This magnitude of uplift and subsidence has been consistent since the onset of hotspot caldera formation at the McDermitt field until the present-day Yellowstone Plateau. As the heat source shifts eastward on the SRP, the crust thermally contracts and sinks (Brott et al., 1981). Age-elevation models and gravity data support the influence of thermally induced subsidence along the SRP axis and margins (Brott et al., 1981). The existing elevation gain from west to east and from the plain margins to the axis also suggests that thermal buoyancy is a mechanism

influencing isostasy on the SRP (Shervais et al., 2005).

Upper crustal temperatures on the SRP (0 - 2 km depth) are generally controlled by the extensive SRP aquifer, which is approximately 95 km by 300 km in areal extent and up to 400 m thick with horizontal fluid flow velocities on the order of ∼1.6 km/yr (Brott et al., 1981; Smith, 2004). Cool aquifer waters control the thermal regime in the Quaternary basalt flows, masking the high heat flow and temperatures of the crust beneath the vadose zone (Brott et al., 1981). The aquifer system is potentially useful for the SRP as a geothermal resource because it could easily provide, over a wide area, the fluid necessary for geothermal heat exchange, but cannot provide the heat for a geothermal resource. High flow velocity in the aquifer enhances convective cooling at the interface between the tuffs and basalt. Potential insulating effects of the basalt are diminished and the steep temperature gradient at the boundary removes energy from the underlying units.

Below the basalts, geothermal gradients in several wells are around 45°C-60°C/km, corresponding to a temperatures of 135°C-180°Cat 3 km (Smith, 2004). Heat flow of 110 mW/m2 below the aquifer is well above values for the Basin and Range region (Brott et al., 1981). Seismicity on the SRP is notably low, and it has been hypothesized that the high temperatures at relatively shallow crustal depths create conditions amenable to plastic deformation or aseismic creep, thus inhibiting seismicity (Brott et al., 1981). Geophysical imaging and geochemical stratigraphy of surgical basalts suggest the presence of a recent 10-km thick layered Miocene-aged mafic intrusion 12 km below the SRP. The mid-crystal sill that is thought to provide a local heat source for the shallow SRP via advection of magmas in the mid-crust and latent heat of fusion from cooling of the sills (Blackwell, 1989; Shervais et al., 2006). Whether an intrusion of this magnitude would replenish heat loss due to the convective cooling effects of the aquifer and conduction out of the system since caldera formation is unknown, but magmatic intrusion and the associated heat transfer mechanisms associated support many high-enthalpy systems (Donaldson, 1982).

1.4 Stress State

Recent GPS surface velocities on the ESRP are thought to show strain rates that are indistinguishable from zero. At -0.1 $\pm$ 0.4 x10^{-9} yr^{-1}, ESRP strain rates are an order of magnitude less than in the Basin and Range Province to the northwest, which is extending at 5.6 $\pm$ 0.7 x $10^{-9}yr^{-1}$ (Payne et al., 2012). While the current stress state is unknown and few studies have attempted to measure in-situ stresses, there is geologic and GPS evidence of the orientation of the stress field and tectonic setting. The discrepancy in plate velocities between the Yellowstone Plateau, which is extending at $\sim$ 3 mm yr^{-1}, and the ESRP, which is extending to the southwest at $\sim$2.2 mm yr^{-1}, suggests a contemporary compressional tectonic setting and time-dependent deformation on the ESRP (DeNosaquo et al., 2009; Puskas et al., 2007).

Volcanic rift zones (VRZ) trending generally NW on the SRP record extension since $\sim$4 ma. The trends of these VRZs - the Great Rift at N45°W and Arco-Big Southern Butte at N40°W - are perpendicular to the least horizontal compression orientation at the time of their formation, indicating a compression-positive σ_3 at $\sim$N45°E (Kuntz et al., 1992). This general stress orientation is also manifested in cinder cones aligned at $\sim$N42°E used in the stress map of the coterminous United States (Zoback and Zoback, 1980). Figure 1.1 contains a locations and orientations of least horizontal compressional stress on the SRP inferred by vent orientation.

Stress magnitudes on the SRP are poorly constrained. One of the few attempts at quantifying the magnitude of stress at depth was performed by (Moos and Barton, 1990) using borehole televiewer data logged from multiple wells at the INEL desert site, including the 3 km deep INEL-1. Due to the absence of borehole breakout over the entire depth, lack of detailed strength measurements for the heterogeneous population of siliceous volcanics, and lack of hydraulic fracturing tests, proper calculations of stress magnitudes were not possible (Moos and Barton, 1990).

One critical statement about the stress magnitudes is that for there to be no borehole breakout, the vertical stress must be greater than the horizontal stresses, where vertical stress is typically the lithostatic pressure or overburden (Moos and Barton, 1990; Stock et al., 1985). As compressive stress accumulates at the azimuth of the S_h direction to cause the spalling responsible for breakout at approximately three times the magnitude of S_H, there is a high possibility

that the horizontal differential stress is rather minimal, or the compressive strengths of the lithologies are greater than the loading (Stock et al., 1985). Considering many boreholes on the SRP do not display breakout, such as the recent deep HOTSPOT boreholes and notably the Kimberly well that also breaches into welded tuffs, a low differential stress could characterize more areas than just the INL desert site (Shervais et al., 2013).

The relative aseismicity of the SRP compared to the surrounding Basin and Range and Yellowstone Plateau can be interpreted as an expression of minimal differentail stress and increased strength from the capping of the tuffs by post-hotspot basaltic volcanism (DeNosaquo et al., 2009). Others have attributed this phenomenon as being a result of a migrating or inactive basalt source or from high temperatures allowing aseismic creep in the crust (Brott et al., 1981).

1.5 Fractures

Fractures are planar discontinuities in rock resulting from brittle deformation in the upper lithosphere. Strength, permeability, electrical resistivity, seismic character, and elastic properties of rock are significantly altered and affected by the presence of fractures (Barton and Zoback, 1992). Fractures create pathways for fluid flow, especially in welded tuffs and other low-permeability igneous rock. Understanding fracture characteristics like distribution and orientation will aid in understanding dynamic reservoir properties, and as such, reviewing fracture formation mechanisms is important. In geothermal reservoirs, extension often maintains permeability, while in the SRP, caldera formation and deposition of ash-flows may be the key.

1.5.1 Existing Fracture Systems

The traditional paradigm associated with exploitable geothermal systems in the Basin and Range is that high strain rates and active deformation reduce the potential for hydrothermal sealing, thus allowing the persistence of fractures that can provide a path for deep circulation (Faulds et al., 2012),. Cores from the ESRP tuff units show abundant secondary permeability features, and borehole televiewer (BHTV) logs record large populations of fractures evenly distributed over the units. Sub-horizontal fractures exist, but fractures with wider apertures tend to strike WSW and dip NNW (Moos and Barton, 1990). The sealing of fractures by precipitation from

hydrothermal waters dramatically decreases in-situ permeability in these units, and also provides evidence of past hydrothermal circulation that may have accompanied caldera collapse. Moos and Barton (1990) observed a correlation between non-sealed fracture zones and thermal anomalies that may reflect fluid flow in or out of the well.

Boreholes in the SRP reveal a range of nonwelded to welded tuffs, and tuffaceous interbeds of air-fall and ash-flow tuffs that would be expected in caldera complexes (Cole et al., 2005; Doherty et al., 1979). Hydraulic conductivities determined for fractured silicic volcanics have a maximum value on the order of 10^{-5} m/s, and tend to increase with porosity (LeCain and Stuckless, 2012). Fluid flow in fractured rocks is likely to be focused along younger faults, not in the matrix, and in-situ tests like slug tests and pumping tests give better estimates of holistic hydrologic properties of an aquifer or potential reservoir than do tests on core samples. Pump tests typically are conducted over a large range of depths, but can be tuned with well packers to find properties of specified units (Smyth and John M. Sharp, 2006). 2.1 lists reported hydraulic conductivities and permeabilities of tuff units from the Nevada Test Site and from three aquifer pump tests performed in deep ignimbrites in INEL-1.

The processes and features associated with rhyolitic caldera formation and collapse are well recognized (Cole et al., 2005). Intra- and extra caldera facies give insight into what may be encountered in a buried caldera system (Wohletz and Heiken, 1992). Association of active geothermal fields with the permeable regions of the large calderas - i.e. the many productive fields in the Taupo Volcanic Zone in New Zealand - indicates the importance of locating permeable ring fault zones when trying to site a geothermal reservoir. We previously noted that the ring faults are mostly sealed based on evidence from INEL-1, Kimberly, and temperatures observed in boreholes, but the higher fracture density of certain zones may still be favorable for reservoir stimulation.

Several studies feature analysis of pre-existing joint systems in outcrops of ESRP-type silicic volcanics at the margins of the plain and beneath the basalts near inferred ring fractures of buried rhyolitic calderas (Moos and Barton, 1990; Shervais et al., 2013). While it is questionable if fracture characteristics such as aperture, length, roughness, dip and connectivity observed at the surface extrapolate linearly to depth due to changing stresses, there have been efforts to predict effective permeability based on surface fracture maps and studies (Manning and Ingebritsen,

1999; Pollyea and Fairley, 2012). Given the effectively uniform and lithostatic stress on the ESRP, near-surface fracture distributions may provide a reasonable estimate of that in the target geothermal reservoirs in the shallow lithosphere.

Analog studies at outcrops examined by geologists could give a first order approximation of the heterogeneity of the buried rhyolites. On the scale of a single ignimbrite flow, which averages 0.5 km^3 for SRP-YP tuffs, there can be unique structural features and lithologic zonation dependent on depositional and post-depositional deformation history. For example, emplacement of Huckleberry Ridge Tuff from the Yellowstone Plateau on top of sedimentary diapirs lead to the formation of $\sim$1 m, post- compaction viscous folds, en echelon tensional fractures, and cm to m wide vertical cooling joints occasionally offset by small-scale shears (Geissman et al., 2010; Millard et al., 2005).Embree et al. (2011) documented and conceptualized these rheomorphic features at the site of the failed Teton Dam near Newdale, ID. Figure 1.3 shows the zones observed in the Huckleberry Ridge Tuff (Embree et al., 2011). Figure 1.4 is a stitched photo of this outcrop. Rheomorphic features may correspond with reservoir permeability heterogeneity and connectivity. Forming conceptual models of a deep reservoir based on outcrops of welded tuff on the margins of the SRP would be relatively easy and affordable as the next step in a feasibility study.

1.5.2 Induced Fractures

Accessing adequate matrix surface area for heat exchange in the subsurface of the ESRP requires reservoir stimulation in order to enhance the conductivity of natural fractures that have been sealed by precipitation of minerals from hydrothermal fluids. Tensile fractures noted in the HOTSPOT Kimberly well have been noted at depth, possibly from the influence of cool drilling fluids creating thermal stresses in the hotter ignimbrites (Shervais et al., 2013). Hydraulic fracturing tests are known to constrain the magnitude of S_h, or minimum confining stress (Hickman and Zoback., 1983). The direction of the tensile fracture is controlled by the remote stress and forms parallel to the maximum compressive stress direction, or S_H. This is the same reason that vents are perpendicular to the minimum compressive stress. The predictable orientation of tensile fractures with respect to the stress directions are useful for reservoir design as we can reliably estimate the orientation and location of new tensile fractures with use of well packers

(Byerlee, 1978). However, if there are pre-existing fractures in a target depth for hydraulic fracturing, it is likely that the stimulation will reactive these fractures in shear, which will be less than the tensile strength of the rock.

Once hydraulic fractures are formed, imaging the geometry of these fractures is an important step in estimating the lifespan of the reservoir. Locating a host fault for earthquakes based on their generated seismic cloud has been shown to be feasible for the initial shock, aftershock, and magma intrusion-induced earthquakes, the latter of which has been resolved onto several discrete fracture surfaces (Carena et al., 2002; Carmona et al., 2010). Recently, microseismics produced by pressure diffusion into a large fractured rock mass (several km^2) near a dam have been used to delineate the location and orientation of several fractures within 10 m for a majority of inferred surfaces (Pytharouli et al., 2011). Such a method would prove invaluable for constraining the distributions of fracture systems in rhyolites as it is generally non-invasive and there are pre-existing wells that could be used to induce seismicity

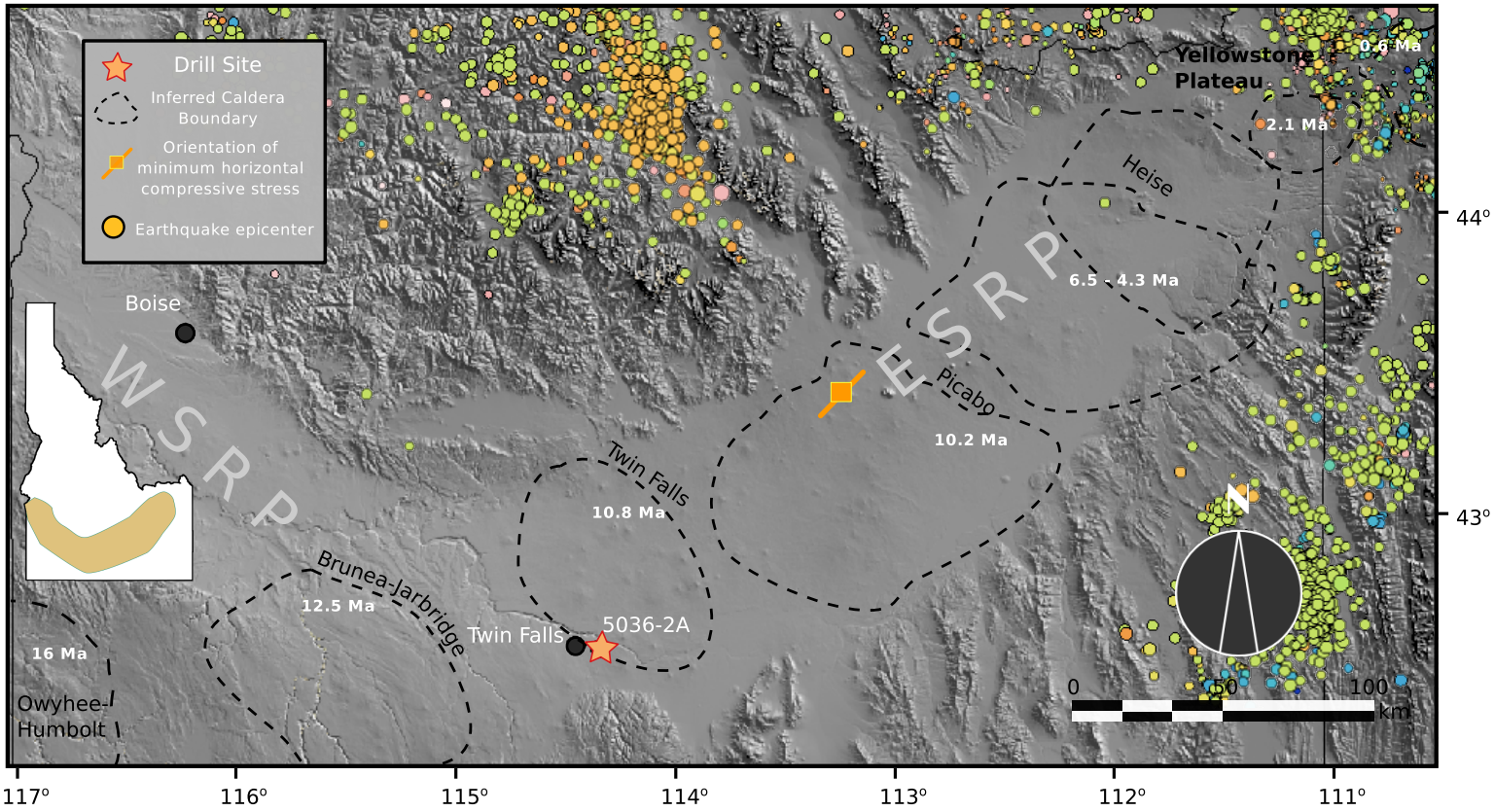

Figure 1.1: Shaded relief map of the Snake River Plain showing broad regional divisions of the Western Snake River Plain (WSRP), a structural graben, and the Eastern Snake River Plain (ESRP), part of the Yellowstone hotspot track. Inferred caldera boundaries are outlined with dashes and the name of the corresponding volcanic fields. These boundaries are often being altered slightly in the literature. Ages of volcanic field activity are well-constrained. The core sampled here was taken from borehole 5036-2A. Orientation of minimum horizontal compression (Sh) on the SRP inferred from volcanic vents on older portions of the SRP, from (Zoback and Zoback, 1980). Earthquake epicenters since 2002 are concentrated in a parabolic shape surrounding the SRP in SE. The Size of the circle is propotional to moment magnitude and color represents depth. Data from Engdahl and Villaseñor (2002)

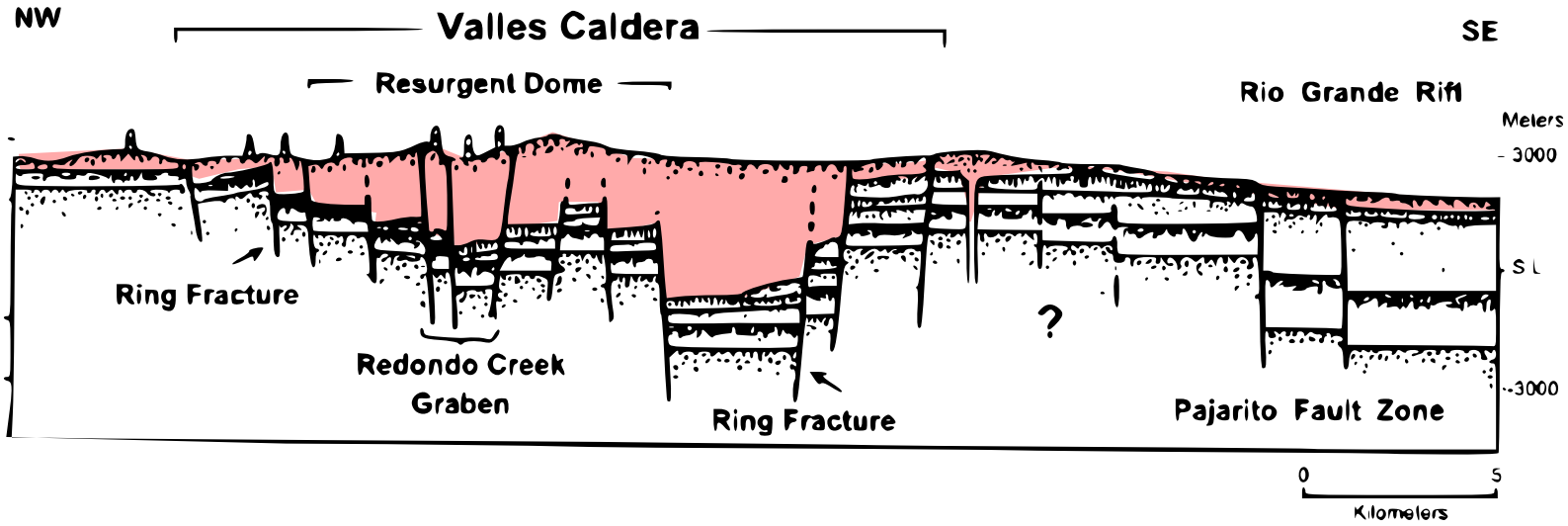

Figure 1.2: Cross section of the Valles Caldera in the Jemez Mountain in New Mexico, from Self et al. (1986). The Valles Caldera is a caldera on the same order of the SRP-Yellowstone calderas. Ring faults and other concentrations of deformation during caldera formation and collapse are host to natural hydrothermal systems and could be targets reactivating pre-existing fractures for an EGS system.

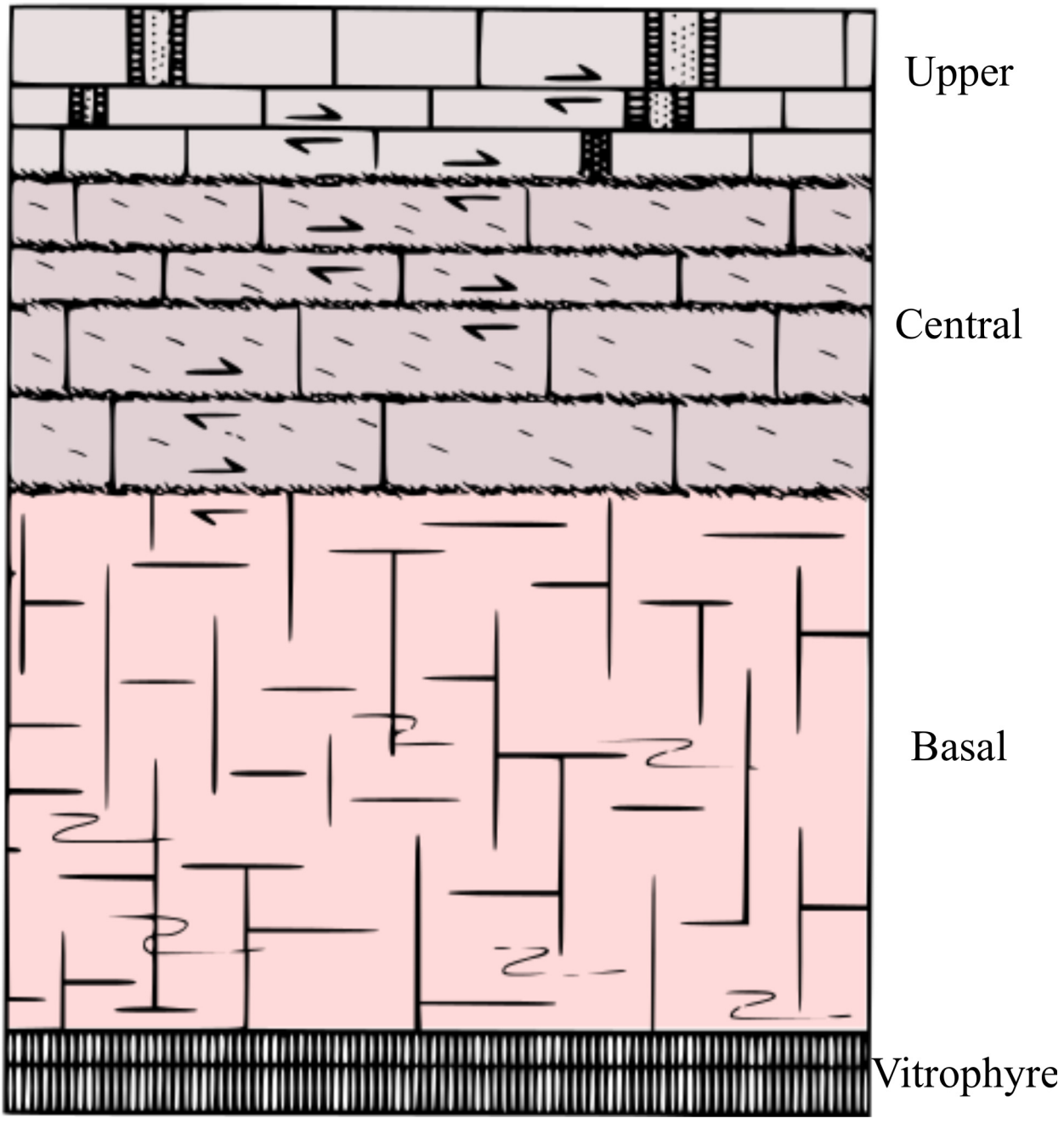

Figure 1.3: Conceptualization of the structural and lithologic zoning exposed in outcrops of Huckleberry Ridge Tuff in Teton Canyon. From Embree et al., 2011.

Figure 1.4: Stitched photograph of welded Huckleberry Ridge Tuff in Teton Canyon just downstream of the Teton Dam failure site to the NE. Fluid flow in welded tuffs will occur along fracture pathways. Inset is a detail of the outcrop showing blocks bounded by near-perpendicular sets of horizontal and vertical fractures.

Chapter 2: Kimberly Core Logging

Data on welded tuff fracture characteristics were gathered from a core produced from the central Snake River Plain near Kimberly, Idaho as a part of ICDP Project HOTSPOT Shervais et al. (2013). The upper core documents basalt flows, intercalated lacustrine sediment units, rhyolite lavas, and brecciated sections before encountering a massive, densely welded tuff from ∼600 m to 1982 m. Prior unpublished work on the core places a fault zone around 960 m from the land surface (Shervais, 2014). Phenocrysts of plagioclase, alkali feldspar, pyroxenes, magnetite, ilmenite, apatite, and zircon occur throughout the silicic lava and tuff units (Christiansen, 2014). The lithologic log is summarized in figure 2.1

To characterize fracture distribution, the Kimberly core was randomly sampled from the length of the lower welded tuff section. A uniformly distributed pseudo-random algorithm native to MATLAB aided in selection of random boxes corresponding to 'core runs'. I noted fracture occurrence with depth, dip, and presence of alteration. To efficiently gather occurrence and dip data of fractures, unwrapped high-resolution core scans were stitched together in the program Corelyzer (Rao et al., 2005) and measured for fracture depth and trough-to-trough amplitude, h. Knowing that length and the core diameter, d, dip is obtained using the relation $atan(h/d)$ (Figure 2.2). The core was not oriented, so noting strike information was not possible.

A preferentially oriented fabric appears to be present in the core above the inferred fault zone at 960 depth. Instead of being oriented perpendicular to vertical lithostatic stress as would be expected in the welding process, the subtle fabric dip is consistent across small depth ranges, but varies significantly over larger scales. Permeability is generally thought to be enhanced along planes parallel to flow emplacement and flattened lithophysae (Fuller and Sharp, 1992). No clasts in the Kimberly core are flattened, and alteration parallel and sub-parallel to the fabric in many zones suggests that previous hydrothermal flow occurred along that fabric.

Core scan analysis presented here represents depths from 660 m to the bottom of the hole, over which 3271 fractures and 2184 dips were observed. Fewer dips were documented because some fractures lacked the distinct sine curve in the core scan needed to allow confident measurement of the amplitude. Inspection of the core showed that the trace of many fractures curved, forming a scooped or undulating fracture surface. Because that curvature was not as

evident in core scans, dip estimates in such cases overestimate the true dip. Scatter plots of all the observed data show no obvious correlations of dip, depth, and fracture spacing (2.5). While data from random sampling and inspection of dispersed core samples was not used to define fracture characteristics, alteration of a majority of fracture surfaces was evident in those samples. Alteration of fracture surfaces indicates that those fractures were not mechanically induced during drilling. In the case that an altered surface does not mark a true discontinuity, we assume that the mechanical discontinuity exploited a pre-existing plane of weakness and is therefore relevant to the fracture distribution that would influence development of an engineered geothermal reservoir.

2.1 Fracture Statistics

2.1.1 Fracture Distribution

Figure 2.4 shows the results of fracture locations collected from the core scans in terms of frequency over the given intervals, N/L, where N is the number of fractures, and L is the sampling length. Histograms of fracture locations with bins of 1 m and 10 m give the corresponding fracture frequencies. At the resolution of fractures per meter, the data is overwhelmed by variance in the data. Viewing the same information at fractures per 10 meters allows for easier viewing of any trends, if they exist. Between 1200 m to 1400 m there appears to be a slight decrease in the fracture frequency relative to the core runs above and below these depths. A histogram and fitted normal probability density function (pdf) of fracture frequency is seen in figure 2.6 with the corresponding parameters. Fracture spacing, unlike fracture frequency, does not follow a normal distribution. Figure 2.6 illustrates the fits of exponential, weibull, and gamma distributions. Each distribution fit gives a mean spacing of $\sim$0.35 m.

2.1.2 Fracture Dip

Dip angles are uniformly distributed between 0°- 90° below the inferred fault zone. There is a steepening trend with depth to the dips when nearing the fault from above. Assuming a normal distribution, the dips above and below the fault are statistically distinct populations. Figure 2.7 displays these two dip populations in histograms that illustrate the acceptable fit to a lognormal

distribution for upper core dips where the mean angle is 23.8°. Lower core dips do not fit a normal, lognormal, or other common distributions, appearing instead to be uniform within the domain. The mean for lower dips is about 46°. Both dip population means may actually be steeper due to under-sampling of steep dips from a vertical scanline, as noted by other authors (Terzaghi, 1965; Hudson and Priest, 1983). Figure 2.5 demonstrates the lack of correlation of fracture spacing with depth and dip. Other investigations note a similar independence of fracture orientation and geometry variables in borehole investigations (Barton and Zoback, 1992).

In order to determine the potential ability for a fracture to host fluid flow, we assume fractures in shear under the current stress state will likely be more hydraulically active due to enhanced permeability (Barton et al., 1995). A normal faulting stress regime is assumed with lithostatic stress from the overlying beds considered to be the most compressive principal stress, σ_1. While the horizontal stresses in the Kimberly borehole are unknown, the strength of the crust allows for lower limits to be set on the minimum compressive principal stress, which is $\sim 0.6\sigma_1$. Figure 2.9 shows a Mohr stress diagram of shear stress versus normal stress acting on each fracture measured in the borehole and provides failure envelopes for pre-existing fracture planes with a coefficient of friction, μ , typical of crustal rocks. Fractures with shear to effective normal stress ratio greater or equal to this typical value of $\mu = 0.6$ are critically stressed and more likely to be hydraulically active. Figure 2.10 displays the distribution of the shear to effective normal stress ratio, or slip tendency, versus depth in the core with the size of the point proportional to the dip. The results are an upper limit estimate of critically stressed fracture occurrence since the core is not oriented and fewer fractures will actually be aligned with the stress field. Nonetheless, a majority of fractures will not be critically stressed and will likely be less permeable under in-situ conditions.

2.2 Geostatistical Background and Analysis

Geostatistics relies on the assumption that a given variable varies in a way that has a structure in space that can be defined by a random function, *Z(x)*. By using measured data, the spatial correlation structure is used to predict values of the variable at unsampled locations. The observed and modeled statistics may also be used to form simulations of alternate variable distributions

that aid in assessing uncertainty in a numerical model via monte carlo-type simulations with all realizations of the reservoir. Stochastic simulation of a geothermal reservoir is the motivation for this chapter in order to address uncertainty of fracture frequency heterogeneity in the Kimberly borehole.

SRP Spatial Correlation

Two prior applications of geostatistical methods for reservoir characterization in the SRP aquifer provided the motivation to use these methods on underlying rhyolite units. Examining regional horizontal hydraulic conductivity on the ESRP, correlation structures based on 79 well tests show anisotropic structures of $ln(K_H)$ oriented north north-west, south south-east with a 4:1 ratio similar to regional volcanic structures (Welhan and Reed, 1997). Correlation ranges are similar to the scale of an individual basalt flow, suggesting cross correlation between lithologic structures and bulk hydraulic conductivity. When more data become available for deep-rhyolite-hosted reservoirs, the geometry of the collapse caldera could be expected to control the direction of anisotropy.

Characterization from a field-based outcrop analog study accounted for vertical and horizontal heterogeneity of permeable structures in a basalt outcrop at INL (Pollyea and Fairley, 2012). The study addressed the uncertainty inherent in analog outcrop studies; incomplete knowledge of basalt-flow distribution at the target depth, by performing stochastic simulation of equally probable reservoir realizations. Subsequent numerical injectivity models were possible by relation of flow-structures with prior air-permeameter permeability studies conducted on the same outcrop. Similar Monte Carlo methods of sequential indicator simulation are used with fracture frequencies in the Kimberly borehole for this paper.

2.2.1 Semivariograms

The experimental semivariogram is an extremely useful measure of spatial correlation and is the basis of all geostatistical models. The purpose of the experimental semivariogram is to measure the average dissimilarity between points separated by a lag distance, h, and is defined by the following equation (Goovaerts, 1997),

$$\gamma(h) = \frac{1}{2N(h)} \sum (z_i - z_{i+h})^2$$

where N is the number of data pairs, z_{i} is the variable value and h is the lag distance. In reservoir modeling, large-scale heterogeneities in the architecture are typically the focus of investigation, yet simple semivariograms tend to smooth out data and result in overestimated low extremes and underestimated high extremes. A common solution is to apply an indicator transform to the continuous data in the following manner:

$$ind_i = \begin{Bmatrix} 1 & if x_i < cut_k \\ 0 & otherwise \end{Bmatrix}$$

and then calculate the experimental semivariogram for the transformed data. Models are fit to the experimental semivariograms in order to define the semivariogram parameters of the range (a) , sill (c), and nugget effect (n). Respectively, these parameters represent the transition distance over which spatial correlation is present, the population variance, and the uncorrelated variance at a distance h=0 that often represents, in physical terms, sub-sample size variability (Isaaks and Srivastava, 1989). Figure 2.11 conceptualizes the creation of variograms from a dataset. Models must be positive definite, thus ensuring unique and real solution, but can consist of a nested set of known positive definite models that suit the modeler's needs. Commonly used models are the nugget effect model, spherical, exponential, Gaussian, and linear. Transitional models used herein are (Deutsch and Journel, 1998)

Nugget Effect:

$$\gamma_0 = \begin{Bmatrix} 0 & if h = 0 \\ 1 & otherwise \end{Bmatrix}$$

Spherical:

$$\gamma(h) = \begin{Bmatrix} 1.5(\frac{h}{a}) - 0.5(\frac{h}{a})^3 & ifg \leq a \\ 1 & otherwise \end{Bmatrix}$$

Exponential:

$$\gamma(h) = 1 - e^{\frac{-3h}{a}}$$

Gaussian:

$$\gamma(h) = 1 - e^{\frac{-3h^2}{a^2}}$$

The nugget effect is typically a constant added to the variogram model, but sometimes data appears to not be correlated at all and takes on a 'pure nugget' model, meaning the variable has no spatial correlation. Spherical models reach the sill quickly and flatten out at approximately two-thirds the range, conceptually representing finite spatial influence of governing mechanisms. Exponential models approach the sill asymptotically and have a range defined at 95% of the sill. Gaussian models are useful for 'extremely continuous phenomena' and are characterized by parabolic behavior near the origin and an inflection point (Isaaks and Srivastava, 1989).

Core data can be collected at a very fine scale relative to the reservoir. Fracture locations from the Kimberly core are on the scale of centimeters, and geophysical wells logs can resolve properties on the order of meters. Therefore, averaging the properties is often the best-practice and the level of averaging, or coarsening, is a choice guided by the goal of the model (Deutsch, 2002). Variogram analysis of a binary categorical transform (0 if no fracture present, 1 if fracture present) resulted in semivariance values of zero for all lags. These results are similar to an extensively fractured rubble zone analyzed by Pollyea and Fairley (2012) in surficial SRP basalts. Such high correlation implies that fracture distribution, and thus permeability, may be treated as isotropic and homogeneous at the sampling scale. However, there was a 0.97 probability that any given location did not have a fracture. Since the core is sampled at every centimeter, this is not surprising and a larger resolution variable describing fracture distribution might reveal correlations that are more relevant to macroscopic hydrologic properties of the

rock. A similar concept is viewed in 2.4 where larger trends are masked by looking at fractures per meter.

Traditional and categorical indicator semivariograms of fracture frequencies, binned at 10-m intervals, reveal correlation structures that change with the indicator cutoff value. The experimental and model semivariograms for the traditional semivariogram and indicator semivariograms in figure 2.12 show several cutoffs where the shape of the curve changes, suggesting changes in generating processes for that range of fracture frequencies. Interpretation of cutoffs is partially subjective and often is chosen with the cutoffs practical significance in mind (Isaaks and Srivastava, 1989). When the spatial structure of permeable zones is of interest, separating high fracture frequencies from low fracture frequencies would be of use. We note four frequency cutoffs of 15, 35, 40, and 45 for fracture frequencies in 5036-2A. Each category has a unique variogram structure that is parameterized in 2.2

Variograms of dips for the whole core and above/below fault sections are plotted in figure 2.13. Dips above the fault zone have a defined correlation structure that suggests that this population of fractures is distinct from the fractures beneath the fault. Variography of slip tendency in 2.14 shows linear spatial trends in the continuous semivariogram, the cross variogram between dip location and slip tendency, and the indicator semivariogram with a cutoff of 0.6. Slip tendency cutoffs greater than 0.6 show no correlation and suggest a pure nugget model.

2.2.2 Discussion

Scatter plots of fracture dip and fracture depth suggests that there is no spatial correlation in fracture frequency, but variograms of fracture frequencies from the Kimberly core exhibit spatial correlation in the traditional semivariogram and several indicator variograms. Models fit to each cutoff show varying spatial correlation structures in each domain. Low fracture frequency cutoffs display different behavior from high fracture frequency cutoffs and are best fit with different model functions, which may represent different generating processes. Whether the observed fracture patterns are due to tectonics, caldera collapse, thermal contraction, hydrothermal alteration, mechanical drilling, or a combination of processes is unknown. Several fracture populations may be overprinted in the core and could be more distinctly identified if strike data were available. We can speculate that the coring process exploited pre-existing planes

of weakness resulting from the current or past stress regime, or that only the pure nugget model representing discontinuous behavior is from coring. However, further data on magnitude and orientation of in-situ stress are needed to predict expected natural fracture geometries. Until then, we cannot separate natural from induced fracture frequencies. Linear trends in the dip and slip tendency variograms may be a result of a dominant lithostatic stress state, as this stress increases linearly with depth.

While geostatistical characterization of fracture frequencies is useful for estimating bulk porosity, corresponding measurements of bulk- or fracture- permeability would improve any estimates of reservoir hydraulic properties. Pollyea and Fairley (2012)'s basalt reservoir simulations would be ideal for heat extraction modeling if appropriate conditioning data for fracture frequencies were available. Lacking equivalent permeabilities for fracture frequencies, we are unable model possible permeability heterogeneity around the Kimberly borehole. Looking to similar studies in welded tuffs, we see that there is no evident between number of natural fractures and air-permeameter permeabilities in Nevada Test Site boreholes (LeCain, 1997). In lieu of data for the Kimberly borehole, fracture and aquifer tests for other deep boreholes, like INEL-1, could be used and will be investigated in further studies.

2.3 Fracture Heterogeneity Simulation

Fracture frequencies can still be treated with stochastic simulation techniques. The schematic in figure 2.15, inspired by Pollyea and Fairley (2012), shows a possible workflow for simulation of reservoir heterogeneity in preparation for numerical modeling of CO_2 injection. First, the modeler chooses cutoffs appropriate to the goal of the simulation. Then models are fit to the semivariograms for those cutoffs and the probability distribution is defined, which determines the spatial variability and areal proportion of each cutoff. A simulation algorithm then creates equally probable heterogenous reservoir with some fluctuation around the semivariogram and probability distribution. The final step is to run flow simulations through each reservoir realization. Lacking permeability data for the welded tuff unit, only facies based on indicator cutoffs can be simulated. Such averaged results may still provide a qualitative sense of the relative permeability of different zones within the reservoir and provide a first-order conceptual model.

Conceptual models of reservoirs reflect the best attempt to tell a convincing and understandable story of the behavior of a reservoir based on available data and heuristics. These stories are useful in guiding our interpretation of model results, but are also prone to biases and uncertainty since they are abstractions of the true reservoir. In the case of the SRP below the aquifer, the conceptual model is subject to limited economic interest in the past. The idea of the deep SRP or similar, previously-unfavorable volcanic areas hosting a geothermal reservoir is relatively new and lacks the breadth of data familiar in oil and gas reservoirs.

Unlike the previous geostatistical studies on the SRP, fracture frequency data collected from the Kimberly borehole is the only data that exists for SRP rhyolites and only allows for 1-D simulation. Using fracture frequency variogram model parameters from table 2.2, a sequential indicator simulation from GSLIB (Deutsch and Journel, 1998) is used to create 100 equally probable realizations of the fracture frequency from the surface to 6 km. We pose the question

> *How far below a given isotherm do we have to drill to be 95% confident that injection would occur in a high-density fracture zone?*

Tester et al. (2006) provided target depths for the 150°C and 250°C isotherms on the SRP of 3.5 km and 4.5 km, respectively. For each simulation, I used a MATLAB script to find the distance from the isotherm to a specific cutoff. A cumulative frequency chart was then made that represents all simulations, and the depth corresponding to the 95^{th} percentile was selected. Results for both isotherms and all cutoffs are shown in figure 2.18 along with estimates from the Well Cost Lite model for drilling cost estimates (Tester et al., 2006).

Depths to drill past isotherms to each cutoff vary with depth. The difference between isotherms for this distance increases with the value of fracture frequency, but the isotherm requiring greater drilling past the isotherm is not constant. Deeper depths and hotter temperatures require smaller drilling distances past the isotherm to reach high fracture zones. However, when fracture frequencies are considered as dimensionless fracture half spacing, x_{ed}, under the flow parameters used in the analytical modeling, they are all the same order of magnitude.

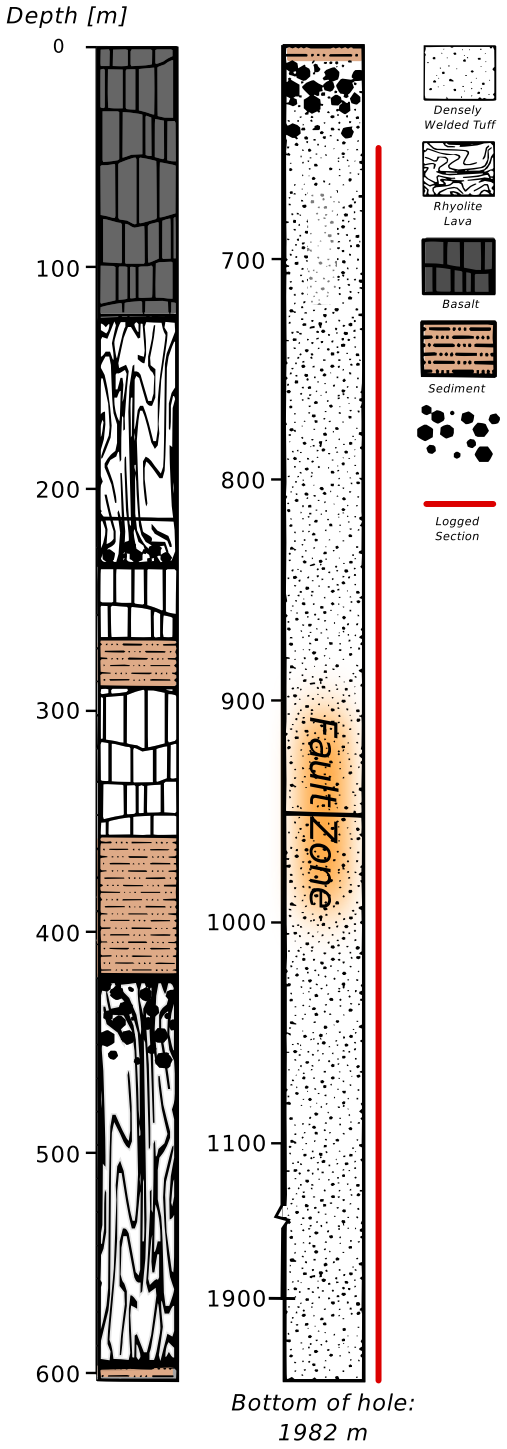

Figure 2.1: Lithologic log of the Kimberly borehole, adapted from Christiansen et al. (2012). Note the jump in the depth scale indicating a large section of welded-tuff. The entire lower unit of the welded tuff was observed for fracture location and fracture dips.

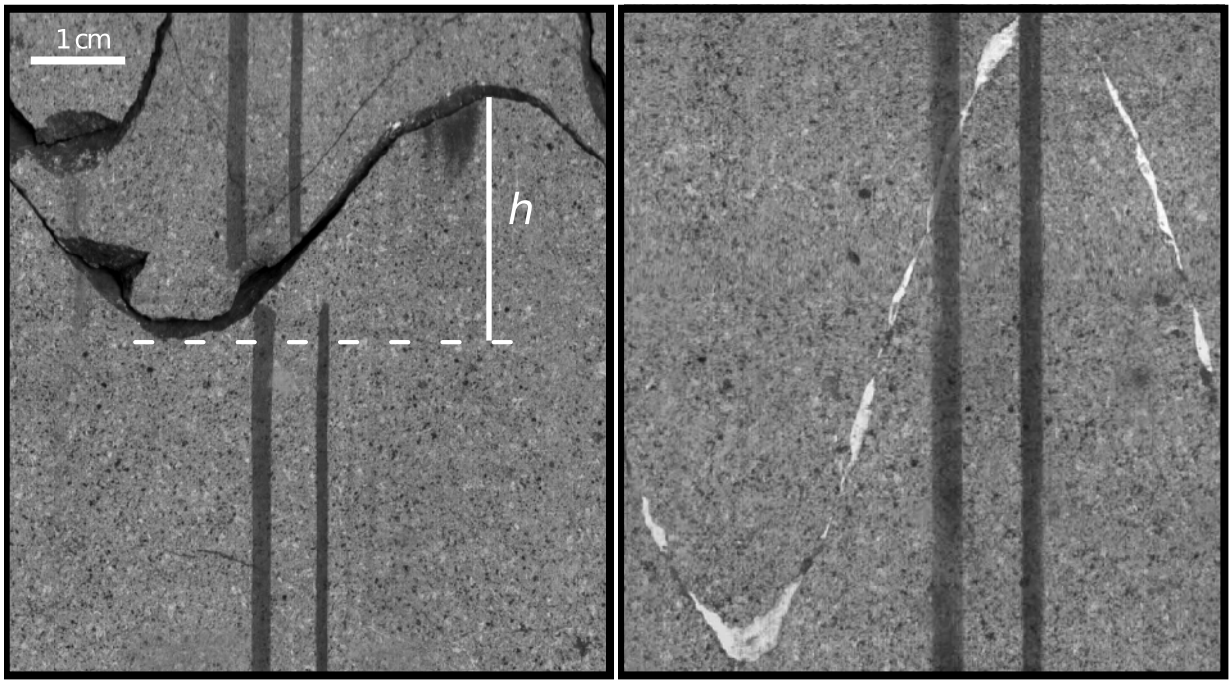

Figure 2.2: Example of 'unraveled' core scan and measurements for determining fracture dip. Fracture locations were recorded as the point where the left side of the scan intersected the fracture. Numerous fractures were sealed, as seen on the right.

Figure 2.3: Alteration on fracture surfaces of welded tuff core. Left) Potential slickenlines on core located near inferred fault. Right) Common alteration seen forming a skin on fracture surfaces.

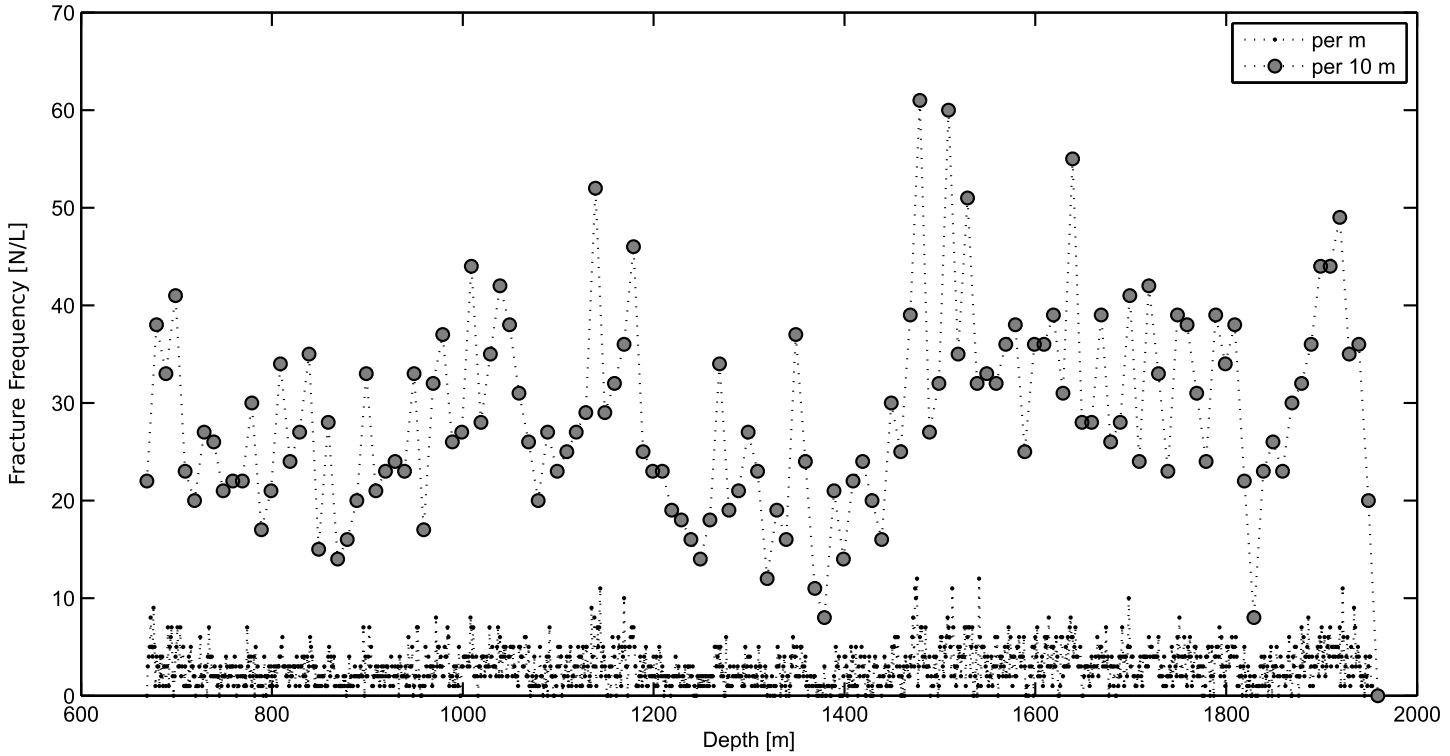

Figure 2.4: Fracture frequency with depth at meter and 10 meter scales. The coarser resolution enhances any trends that may be present

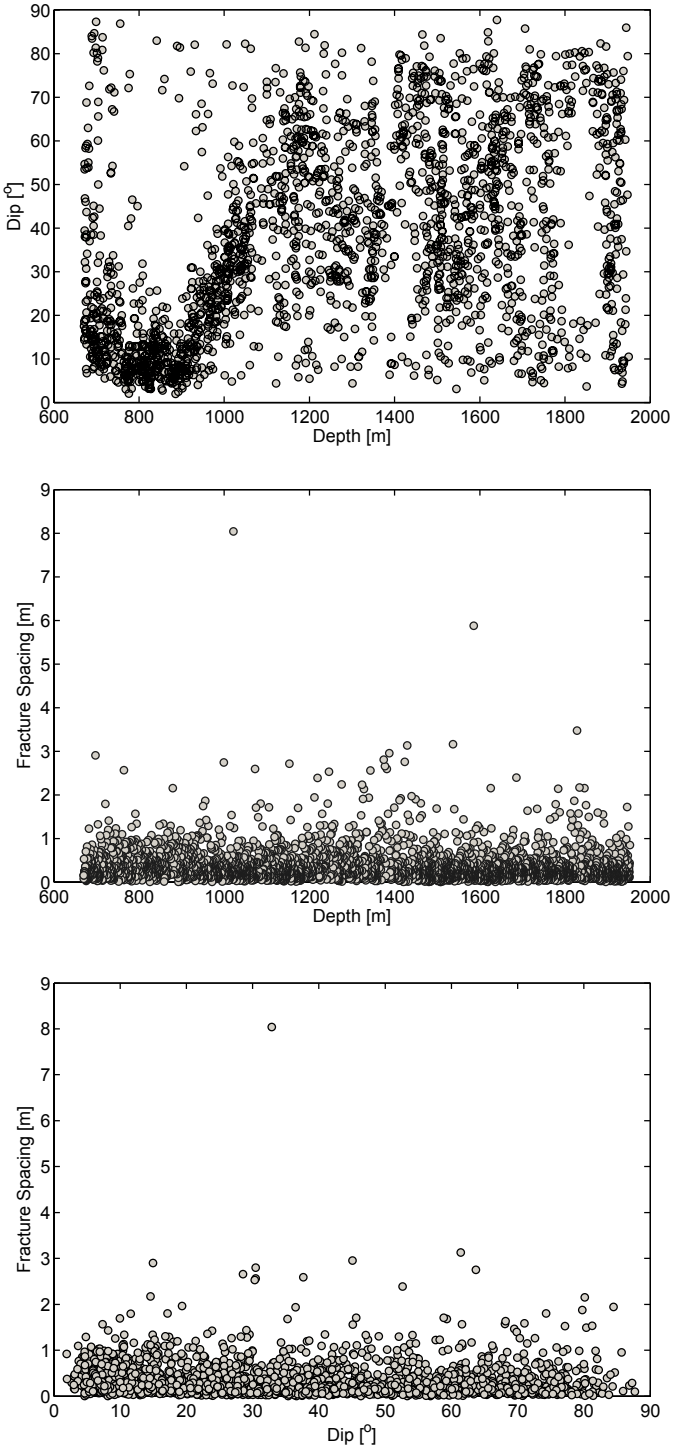

Figure 2.5: Dip, fracture spacing, and depth scatter plots

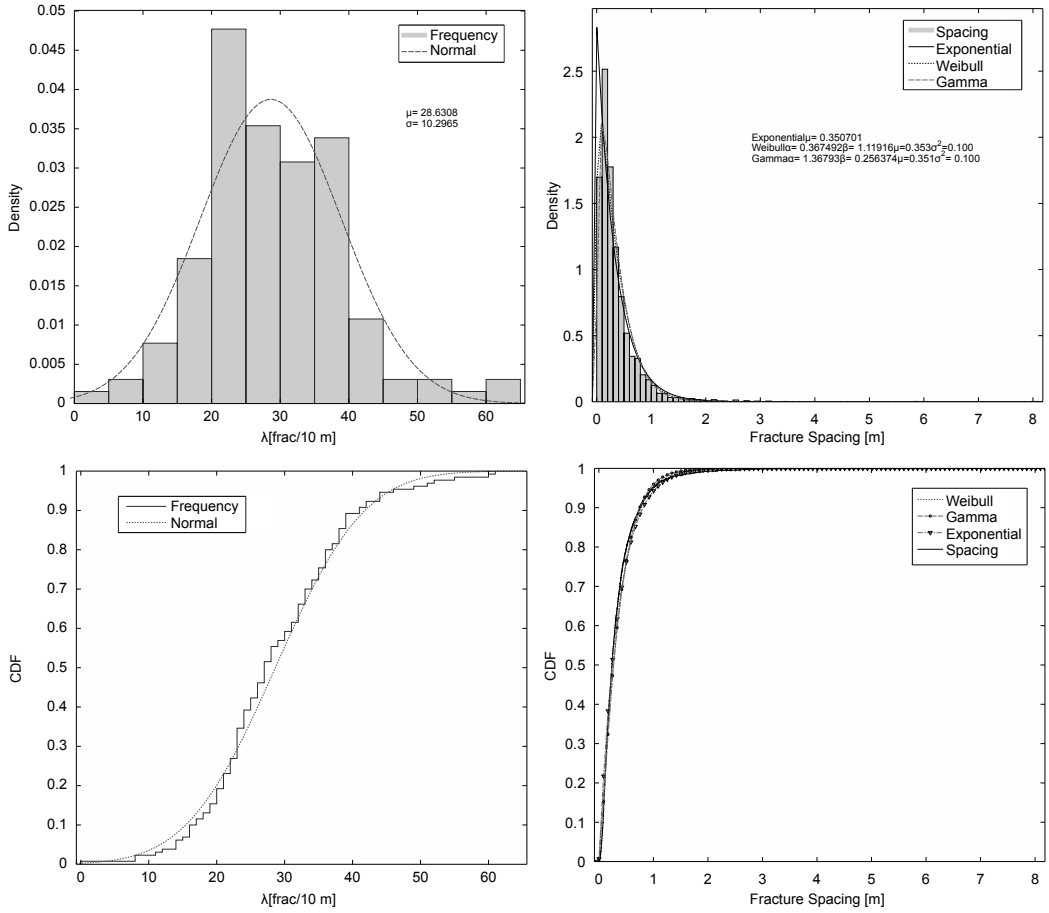

Figure 2.6: Histograms and cumulative frequencies with fitted distribution curves for (left) fracture frequency per 10 m and (right) fracture spacing.

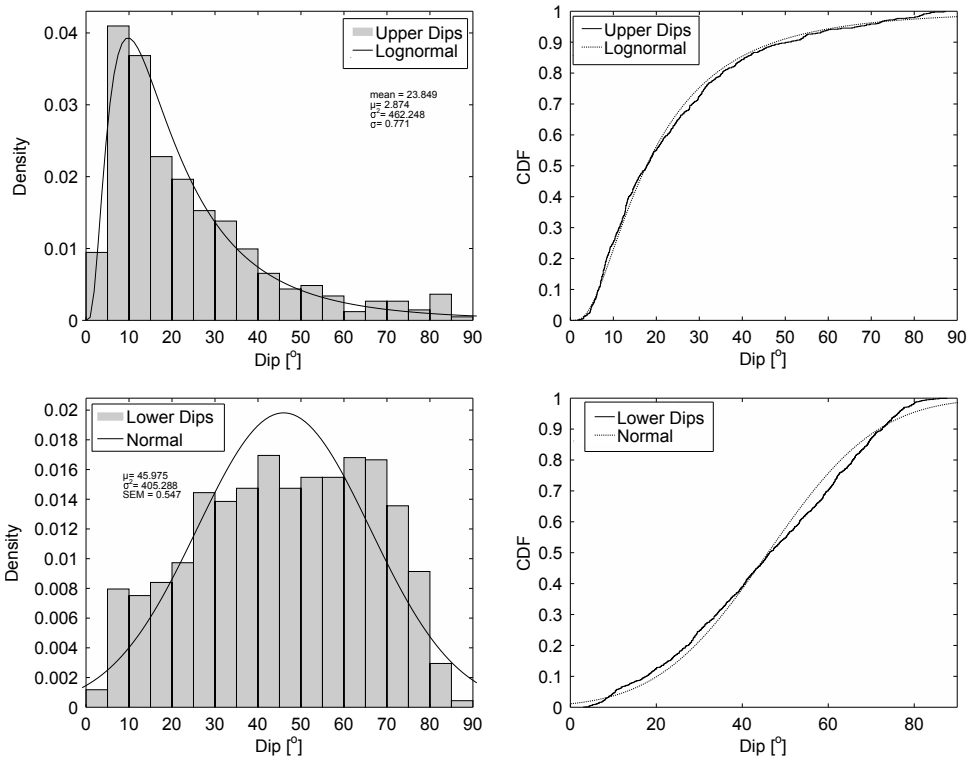

Figure 2.7: PDFs and CDFs for upper and lower section dips and fitted distributions.

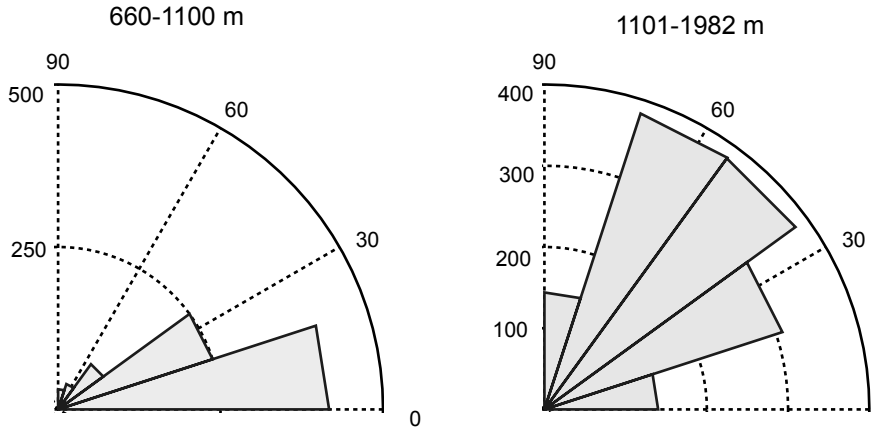

Figure 2.8: Rose diagrams of dip in upper (660 -1100 m) and lower (1101-1982 m) sections of the core. Upper core fractures cluster around shallower dips.

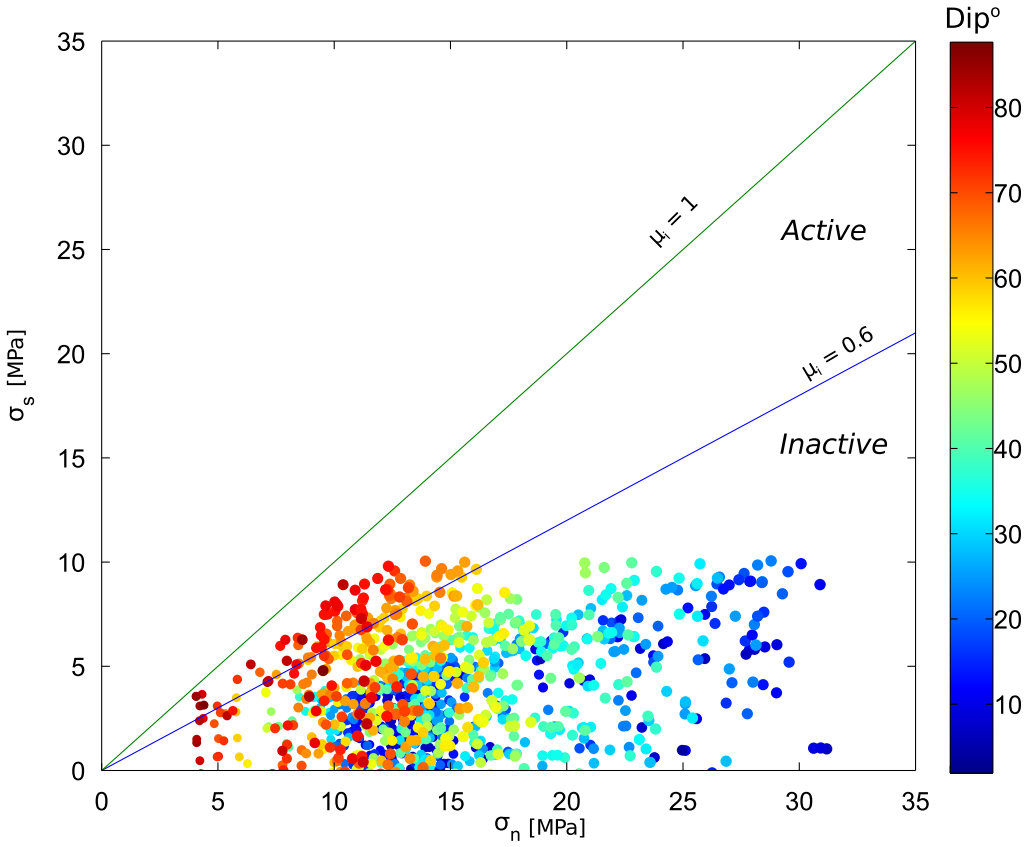

Figure 2.9: Normal stress vs. shear stress on pre-existing fractures in the Kimberly core if they were oriented with the three principal stress directions in a normal stress regime. Fractures falling above the $\mu_i = 0.6$ line are critically stressed and would be more likely to be hydraulically active.

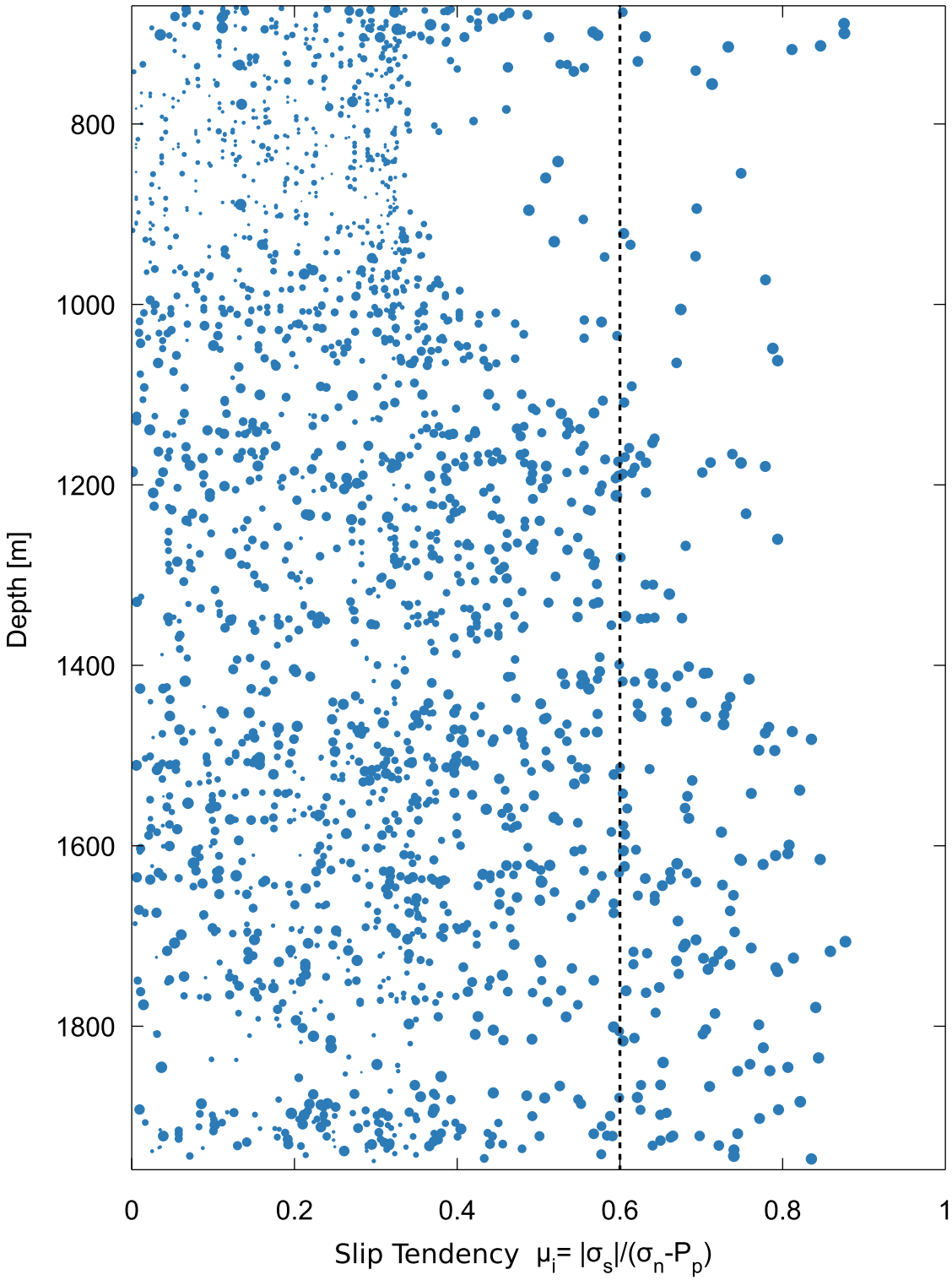

Figure 2.10: Slip tendency for each fracture hypothetically oriented with the stress field.

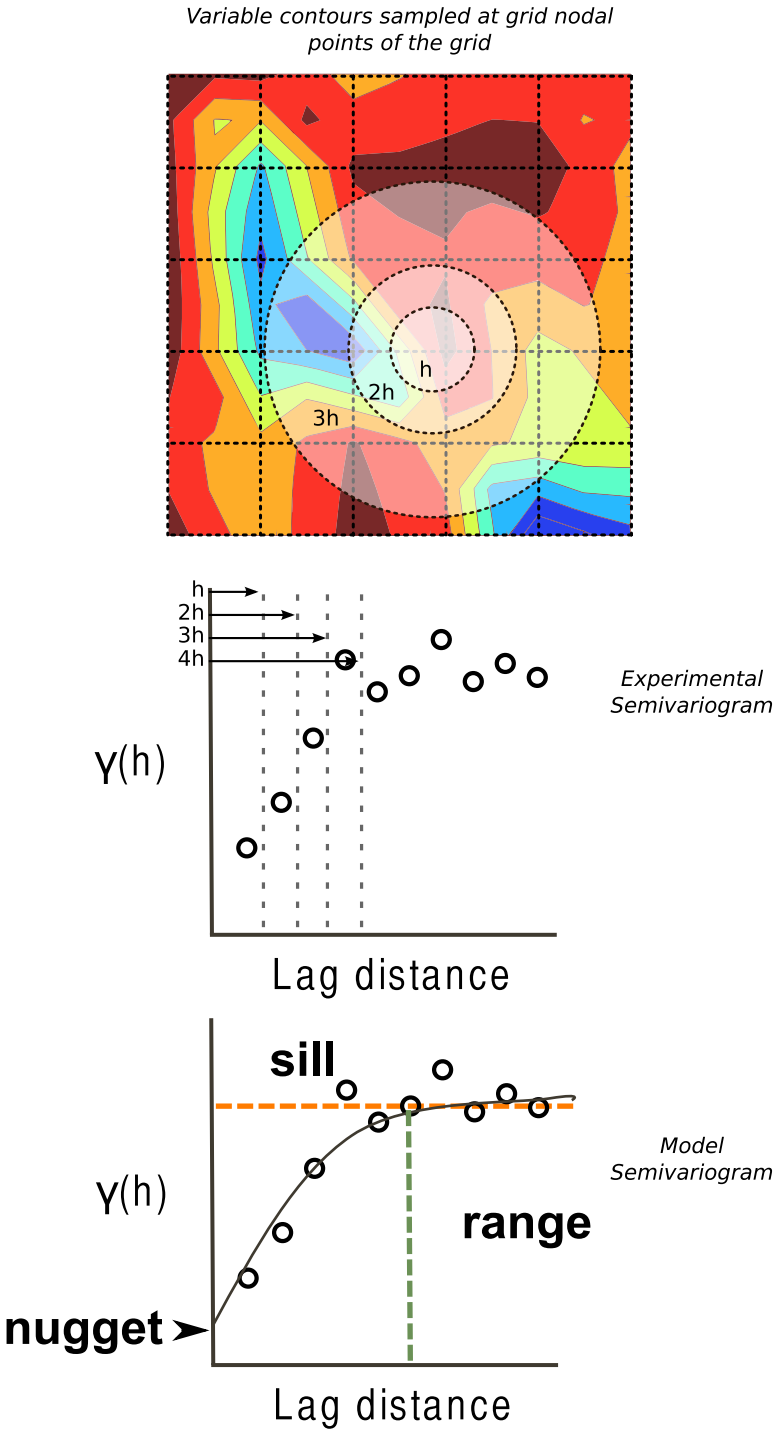

Figure 2.11: Steps to making a model variogram for a dataset. Top) Data are collected at a certain resolution, shown here by the orthogonal grid. Experimental variograms are made by selecting a lag distance h, averaging the semivariance for all data points in the dataset separated by that distance, and continuing for multiple of that lag distance. Middle) Example of an experimental semivariogram. Bottom) A model is fit to the experimental semivariogram in order to define range, sill, and nugget effect.

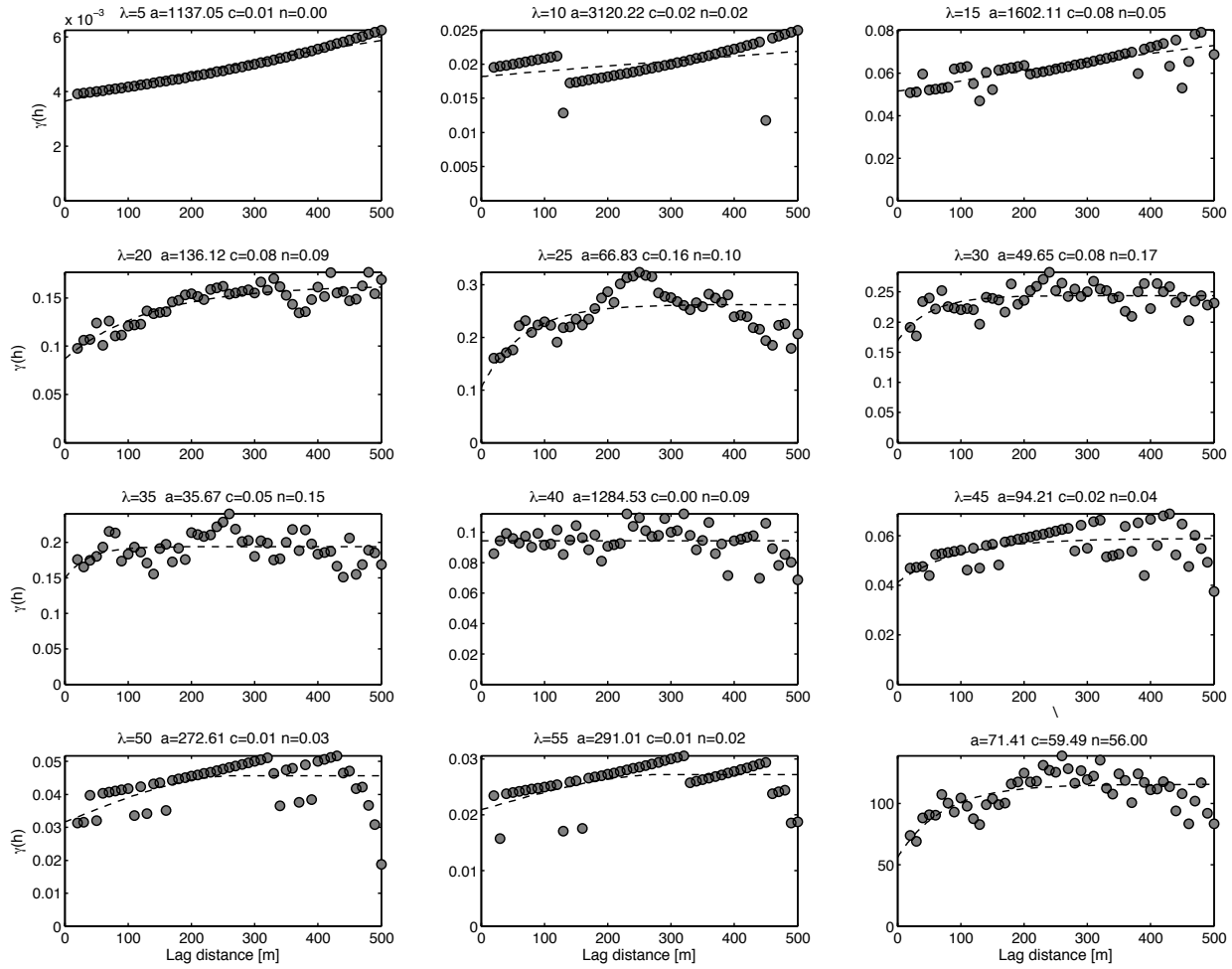

Figure 2.12: Variograms of fractures/10m for the Kimberly core. The bottom right variogram is a traditional semivariogram of all the data. All others use indicator cutoffs to find correlation of ranges of fracture frequencies. A change in curve shape indicates a change in correlation at the given cutoff. Cutoff (k), range (a), sill contribution (c) and nugget(n) values are given at the top of each variogram.

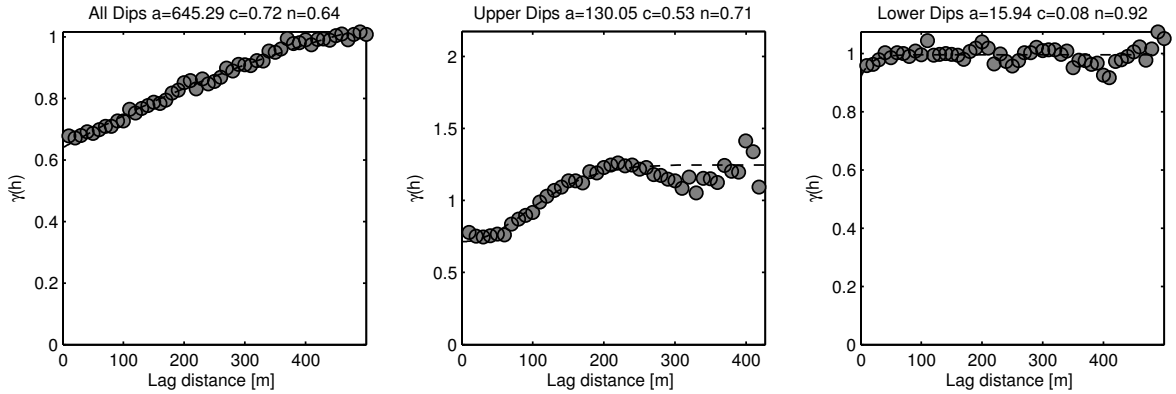

Figure 2.13: Experimental variograms of (left) all dips modeled, (middle) dips above the fault, and (right) dips below the fault. The set of all dips is modeled with a Gaussian variogram, and the smaller set above and below the fault are modeled with an exponential variogram models. Lower dips are mostly pure nugget and show little spatial correlation. Range (a), sill contribution (c) and nugget (n) values are given at the top of each variogram.

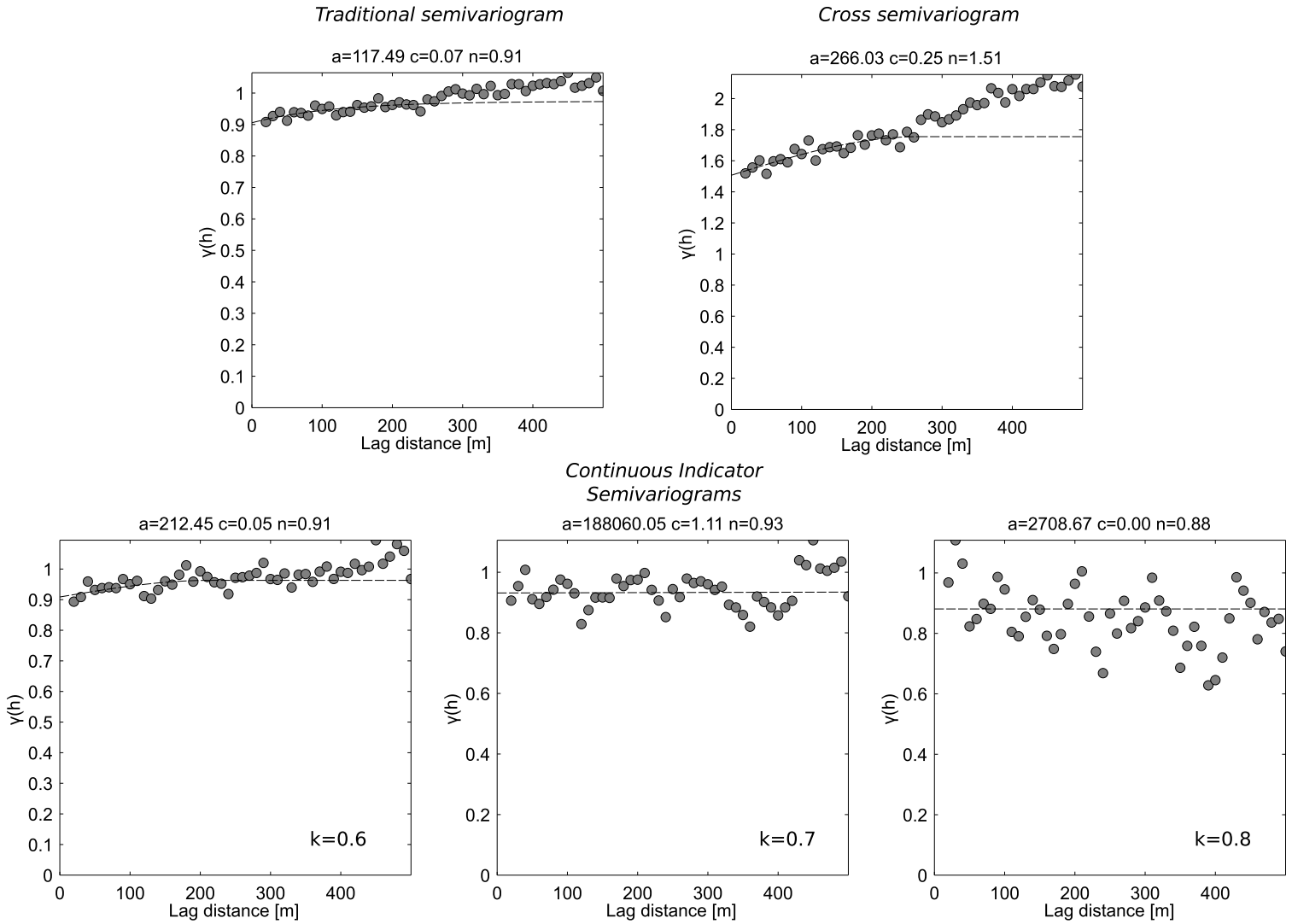

Figure 2.14: Experimental variograms of critically stressed fractures. Top) continuous semivariogram and cross semivariogram, which compares spatial correlation of slip tendency with dip angle. Bottom) Indicator semivariograms at cutoffs of 0.6, 0.7. and 0.9.

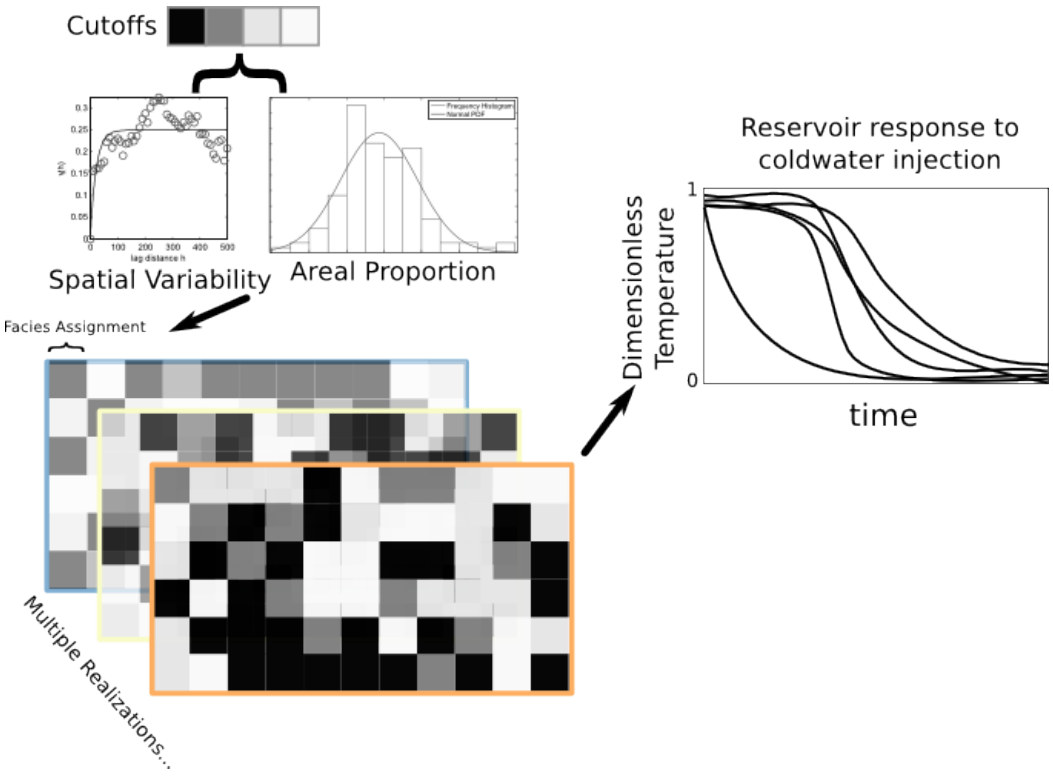

Figure 2.15: Schematic for using spatial data correlation to create stochastic reservoir heterogeneity simulations. These simulations can be used for fluid flow and heat transfer modeling to give a bound on expected behaviors of a reservoir.

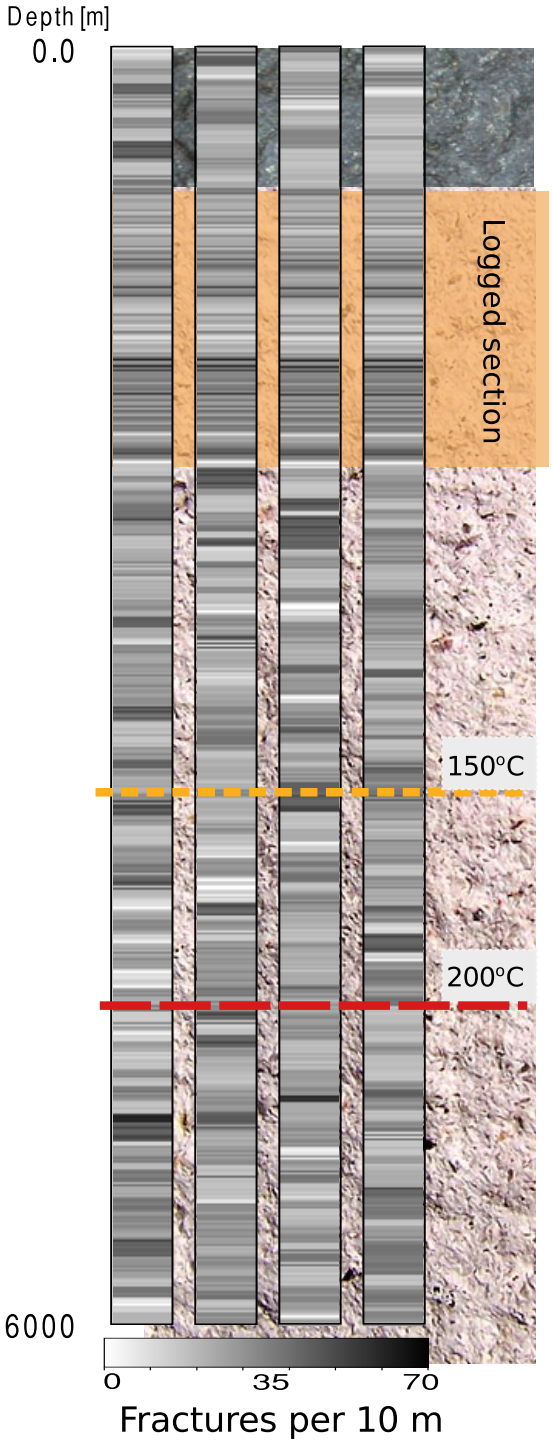

Figure 2.16: Sample realizations of fracture frequency heterogeneity simulated to 6 km depth. Realizations were accomplished using a sequential indicator simulations program in the geostatistical package, GSLIB.

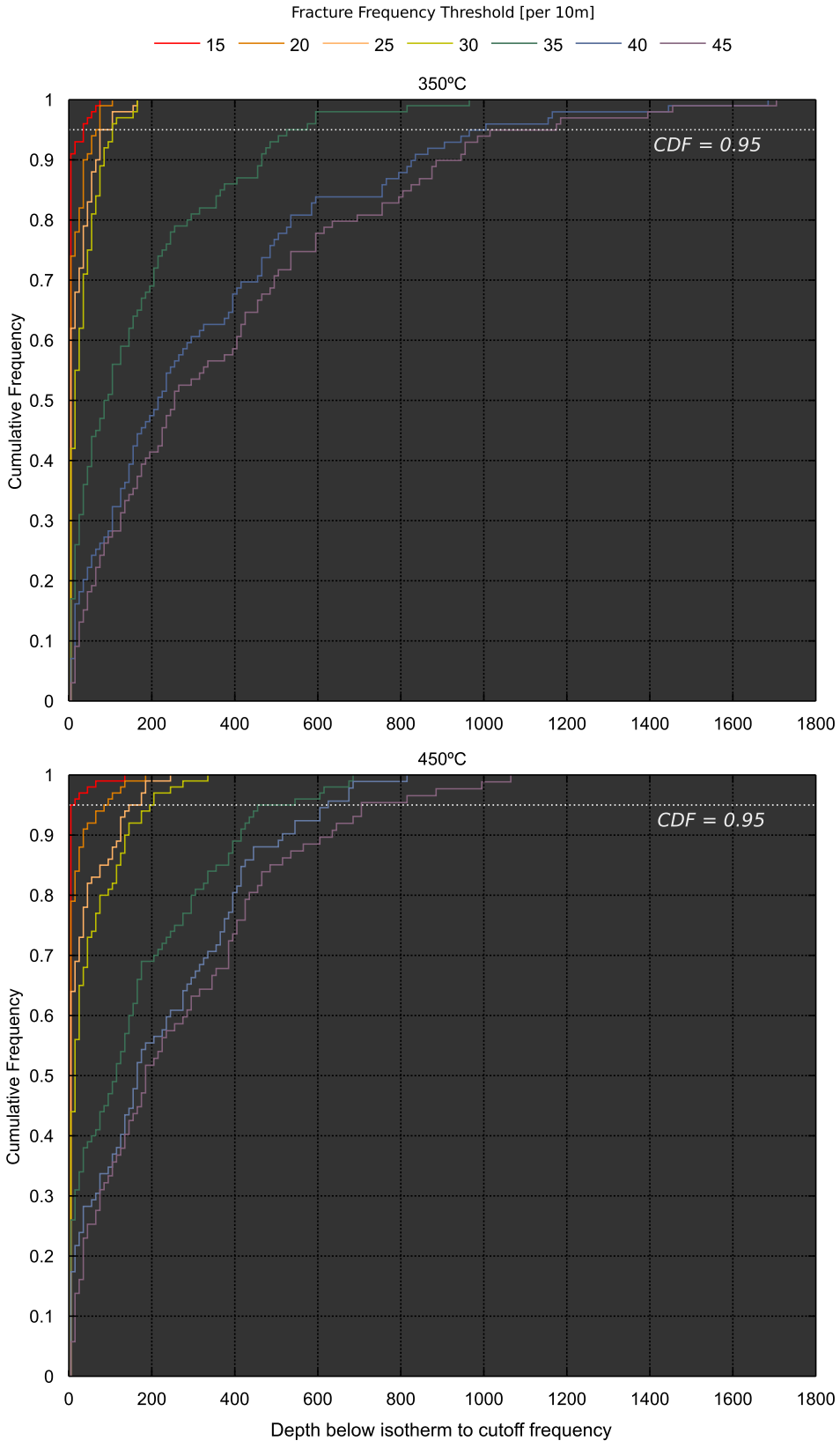

Figure 2.17: Cumulative frequency of simulated depths to a given fracture frequency cutoff for different depths corresponding to isotherms above the graphs.

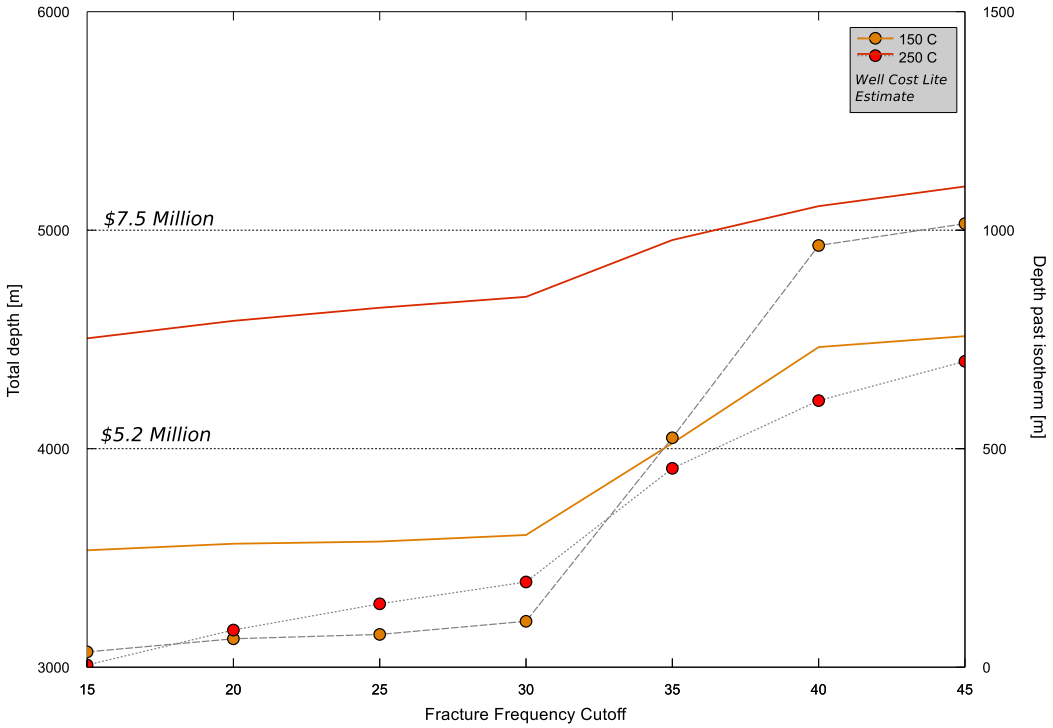

Figure 2.18: Sequential indicator simulation results showing depth past isotherm and total depth to drill to reach a given high fracture frequency zone. Drilling cost estimates from the Well Cost Lite model are from Tester et al. (2006).

Table 2.1: Hydraulic Properties of Fractured Welded Tuff [APT =Aquifer pump test; AIT = air injeciton test]

Sample Location	Degree of welding	Permeability m^2	Hydraulic Conductivity (m/day)	Method	Source
USW H-4	Variable	-	1.2	APT	Whitfield et al. (1985)
USW H-5	Highly Fractured	-	1.0	APT	-
USW H-6	Highly Fractured	-	2.2	APT	-
USW G-4	Variable	-	1.6	APT	Lobmeyer (1966)
USW G-4	Variable	-	3.00E-02	Slug	-
TS	Dense	1.80E-12	1.5	AIT	LeCain (1977)
TS	Dense	4.70E-12	4.0	AIT	-
TS	Dense	2.10E-12	1.8	AIT	-
TS	Dense	4.00E-13	3.40E-01	APT	-
UE-25b#1	Variable	-	4.50E-01	APT	Lahoud et al. (1984)
UE-25p#1	Highly Fractured	-	4.70E-01	APT	Craig and Robinson (1984)

Table 2.2: Summary of Variogram Parameters

Cutoff	CCDF	Range	Sill	Nugget	Model
15	0.09	2700	0.08	0.05	Exponential
20	0.2	136	0.08	0.09	Exponential
25	0.36	67	0.16	0.10	Exponential
35	0.73	35.7	0.05	0.15	Exponential
40	0.86	1.0	0.0	0.09	Nugget
55	0.99	303	0.01	0.02	Gaussian
Traditional	N/A	65.78	0.81	0.41	Exponential

Chapter 3: Heat Extraction Modeling

3.1 Analytical Model

Analytical solutions to heat extraction processes - i.e. (Carslaw and Jaeger, 1959) - are widely used in reporting geothermal potential and for thermal drawdown of the reservoir (Axelsson et al., 2001; Tester et al., 2006). Such models conceptualize the reservoir as a single fracture zone, so that heat exchange occurs only with the rock adjacent to, and not within the fractured zone. Reservoirs are, however, likely to consist of several fractures with interacting cooling fronts, necessitating the use of more complex mathematical treatments. Gringarten et al. (1975) solved the extraction of thermal energy from a rock matrix with multiple fractures interacting cooling fronts, conceptualized in figure 3.1. The 2-D transient advection-diffusion model (see appendix) is semi-analytical and is solved with a numerical Laplace inversion code in MATLAB adapted from de Hoog et al. (1982) for the purposes of this paper. Outlet water temperature as function of distance along the fracture path and time, T_{wd}, is expressed in Laplace space as

$$T_{wd}(z_D, s) = \frac{1}{s} \exp(-z_D s^{\frac{1}{2}} \tanh(\frac{\rho_w c_w Q x_e}{2K_R H}) s^{\frac{1}{2}}) \tag{3.1}$$

where ρ_w is the density of water [kg/m^3], c_w is the specific heat of water [J/K], Q is volumetric flow rate per fracture per unit length in the y-direction [m^2/s], x_e is fracture spacing, $K_R$is the thermal conductivity of the rock [W/m^{2}K], H is an arbitrary length, and s is a Laplace parameter. The geothermal gradient is neglected in our calculations and thermal properties of the rock and water are assumed constant with temperature and location. Reservoir parameters include flowpath length, fracture spacing, fracture aperture, number of fractures, and initial reservoir temperature. Production dictated parameters are mean velocity and fluid injection temperature.

3.2 Model Behavior

The model is derived with non-dimensional parameters and the decline of the water outlet temperature can be understood by examining these parameters. Dimensionless time, dimensionless half-fracture spacing, and dimensionless temperature used by Gringarten are

$$t_d = \frac{(p_w c_w)^2}{K_R \rho_r c_R} (\frac{Q}{z})^2 t \tag{3.2}$$

$$x_{ed} = \frac{\rho_w c_w}{K_R} (\frac{Q}{z}) x_e \tag{3.3}$$

$$T_{wd} = \frac{T_w(z,t) - T_{wo}}{T_{ro} - T_{wo}} \tag{3.4}$$

$Q_v[L^2/t]$in Gringarten is the volumetric flow rate per fracture per unit width of the fracture in the y direction. The total production flow rate is divided equally amongst all parallel fractures such that fracture $= Q_v/(byk)$ where b is fracture aperture, y is the aquifer thickness and k is the number of fractures. Adding fractures to the system effectively lowers the fluid velocity through each fracture as total flow is partitioned among more pathways.

Type curves in figure 3.2 show the reduction of water outlet temperatures for various fracture spacings. For small x_{ed}, the thermal cooling front arrives at earlier dimensionless time as an almost instantaneous drop in temperature occurring once the thermal front arrives. The 'uniform energy sweep' of the reservoir, as in Bodvarsson and Tsang (1982), occurs once thermal disturbance reaches the no-flow boundary between two fracture domains. Large x_{ed} extends the time until the arrival of a cooling front, but for any $x_{ed} >\sim 10$, the cooling behavior is essentially that of independent fractures. This is because cooling within that interfracture distance is effectively complete before the cooling fronts traveling perpendicular to the fracture faces interact, and conduction from distances greater than that spacing is effectively negligible. Departures from the independent fracture cooling curve occur because of this 'late time' behavior, where the rock is cooled completely to the mid-plane, seen in figure 3.3

It should be noted that except when x_{ed} , or the number of fractures, is large, the Gringarten solution for multiple fractures generally overestimates the rate of thermal decline because it assumes each fracture is part of an infinite set of parallel fractures of constant spacing. In the cases considered here, the number of fractures is finite, so the outermost fractures effectively have infinite x_{ed} on one side. Because of this, a small number of closely spaced fractures may effectively behave as a single fracture, with most of the heat provided by the region outside the fractured zone.

Design of a reservoir scheme uses these behaviors to choose an appropriate flow rate and well spacing. The arrival time of thermal drawdown is proportional to the square of the flow rate. The dimensionless fracture spacing when this occurs is proportional to the flow rate. Longer reservoir usability is accomplished by dividing flow among numerous fracture spaced such that heat is extracted in a manner where the arrival of the cooling front is gradual.

3.3 Kimberly borehole optimization.

If we assume that the fractures observed in the Kimberley borehole have sufficient permeability to allow flow, we can calculate the heat recovery that would occur where flow extends through a welded tuff reservoir. To examine how measured fracture characteristics might influence geothermal energy recovery from the SRP, we consider a series of fracture flow scenarios using the Gringarten solution. That is, we assume that water is injected in one well and produced at another (dipole), but consider only the heat exchange that would occur in the idealized system of parallel fractures described by Gringarten. Calculated heat recovery is per unit height of the fractured reservoir. Certain design parameters must be set before determining optimal flow rates and fracture areas for a given host rock. In applying the model to a hypothetical EGS site on the ESRP, production targets are set at Q = 0.063 m^3/s (1000 gpm) for 20 years with a fluid temperature of 60°C. The breakthrough time is defined as the arrival of the isotherm that is half of the initial reservoir temperature. The fracture spacing half-width of such a system can be taken as half of the exponential mean of the fracture spacing data, 0.176 m. The corresponding dimensionless variables are $T_{wd} = 0.5, t_d = 9.37E-4$, and $x_{ed} = 2.40E-4$

Thermal breakthrough occurs after 10.3 years, and the reservoir is completely cooled around the well within just a few months. The sharp drop in temperature recorded in figure 3.4 is expected for such small dimensionless variables. For densely fractured in-situ fracture distributions, this is a reasonable result. With 3500 fractures in the model domain, flow velocity in each 1 mm fracture is 3.6E-4 m/s, allowing conduction from the small volumes of rock matrix to the fracture to completely remove energy in the rock.

Not all fractures will host fluid flow, with roughly one in ten being viable fluid pathways. Figure 3.5 illustrates the results of reducing the number of fractures to 350 and increasing

fracture half-spacing to reflect this reduction in fracture density. Flowpath length and fracture width in the y direction are altered and the corresponding surface area for 350 fractures is noted underneath the temperature curves. One interesting feature of such a parameterized study is observing how lower aspect ratios (i.e. fracture width/flowpath length $\sim$1) increase the time until thermal breakthrough for a given heat exchanger surface area.

3.4 Discussion

Pragmatic reasons dictate designing a system that resists flow as little as possible, thus minimizing the pressure drop required between injection and production wells and decreasing operation costs and demands on the pumps. A reservoir with a low aspect-ratio and flow divided amongst several fractures in a manner that reduces the chance of cooling fronts reaching the mid-plane between fractures will maximize the heat exchanger surface, maintain close well spacings for pumping purposes, and allow for longer production from a given volume of rock.

In the application of the Gringarten model to the fracture distributions observed in the core, we are assuming that all fractures are fully connected and conduct proportional amounts of fluid flow. Such a uniformly spread conduction is unlikely in fractured crystalline reservoirs where in-situ apertures vary widely and fractures with larger apertures will host a major volume of flow. The applicability of a set of parallel plate fractures may be more appropriate to fluid and heat transport in layered sedimentary or volcanic units with more prevalent flow contacts. Doe et al. (2014) used equivalent numerical simulations to assess the effects of variable apertures and fracture spacing. Lognormal fracture aperture distributions and variable spacing reduces the extraction efficiency of flow through multiple fractures due concentration of flow in fewer fractures that limits the occurrence of interacting cooling fronts from adjacent fractures.

Though numerical models like discrete fracture networks (DFN) and finite difference methods can incorporate irregular fracture geometries more easily, the data to fully define these properties over scales of interested is limited and expensive (Neuman, 2005). Characterization of flow in fractured rocks is regarded as a one of the more challenging frontiers of hydrogeology (Faybishenko and Benson, 2000). Develop continues on new techniques combining different approaches to approach a full understanding of the dynamics

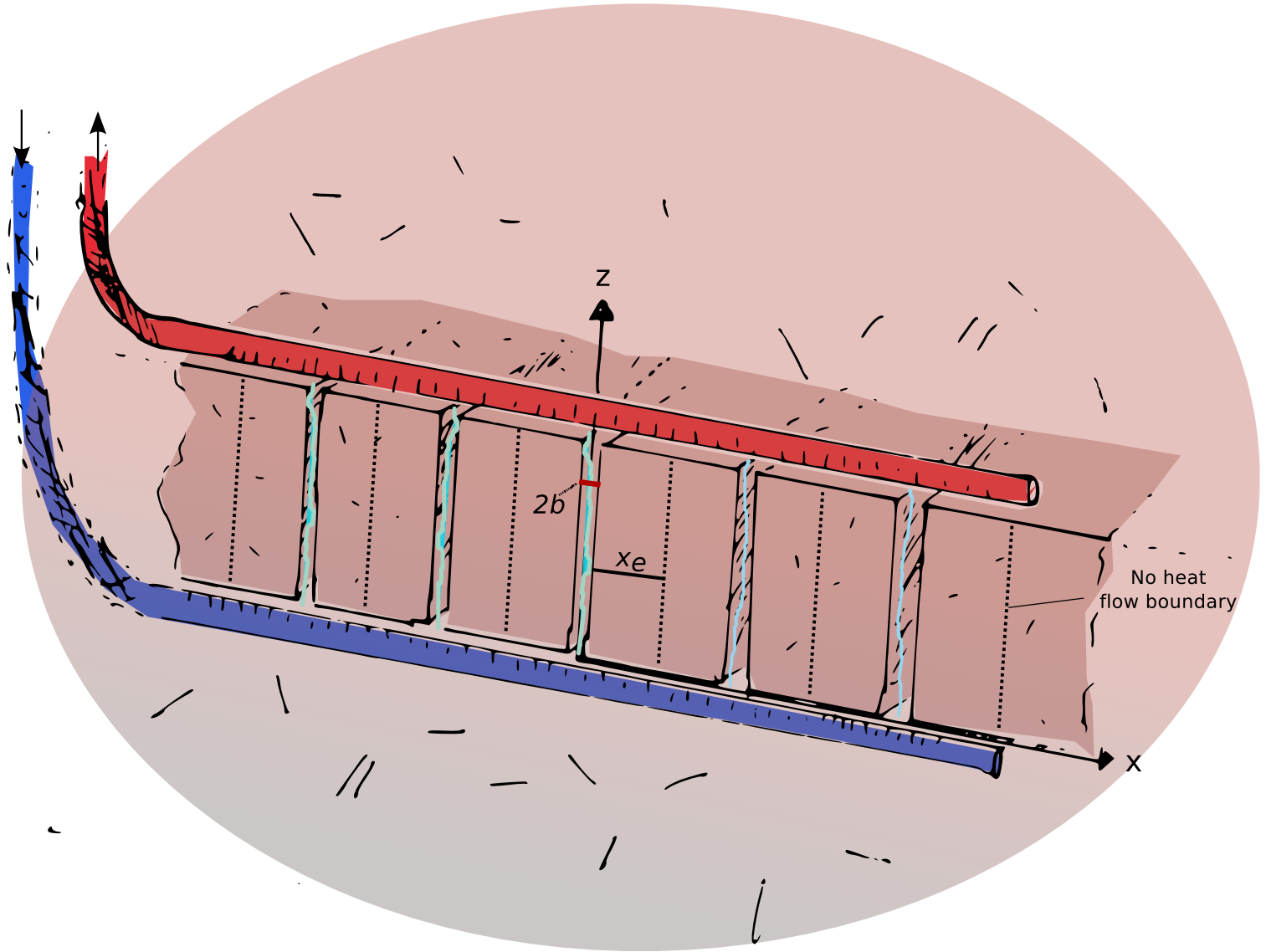

Figure 3.1: Gringarten et al. (1975)'s conceptual model of the multiple parallel plate fractures in a geothermal reservoir. b is the fracture aperture, xe is the fracture half spacing, and water flows through fractures in the z-direction. Model is applied per unit thickness of the reservoir in this paper.

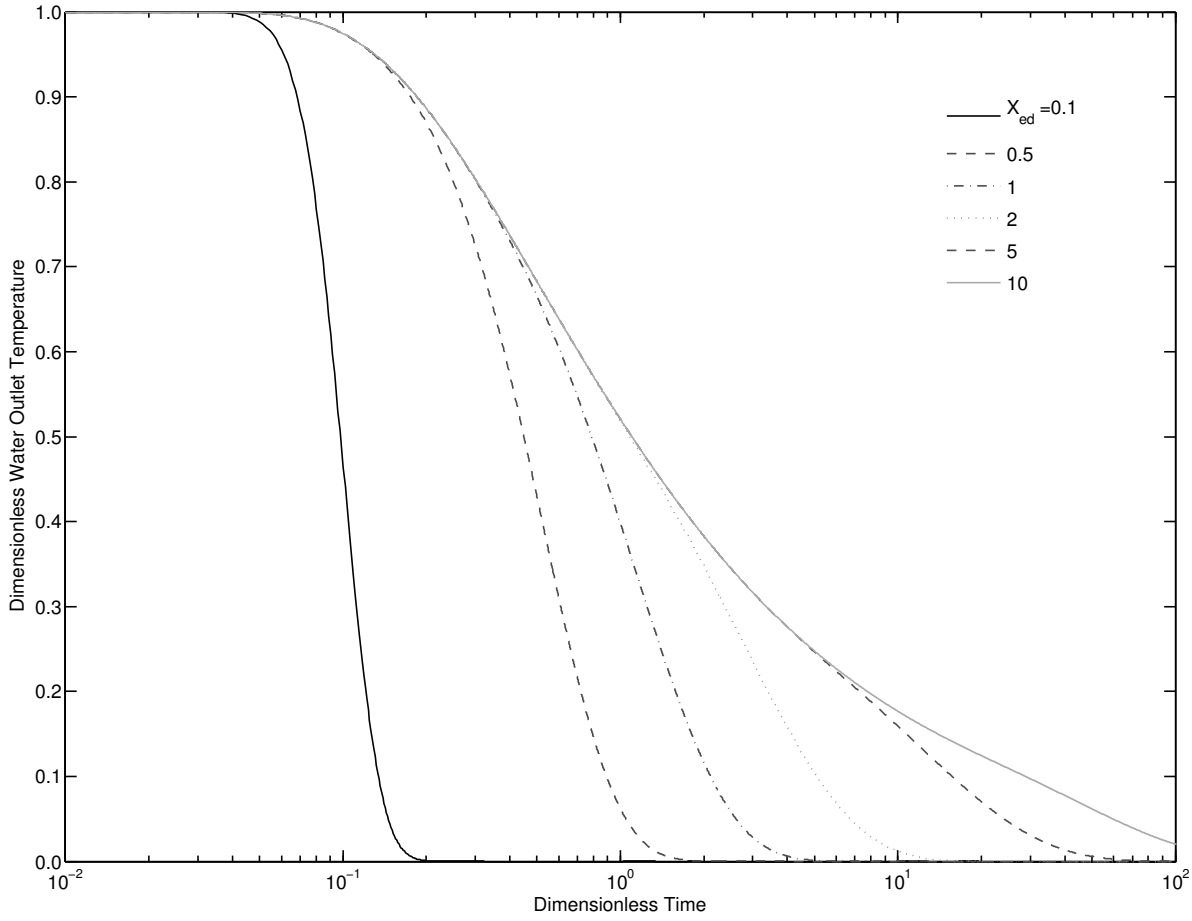

Figure 3.2: Drawdown of reservoir temperature as a function of dimensionless time and half-fracture spacing, x_{ed}. Each curve maintains the same dimensions for the rock volume and flow rate.

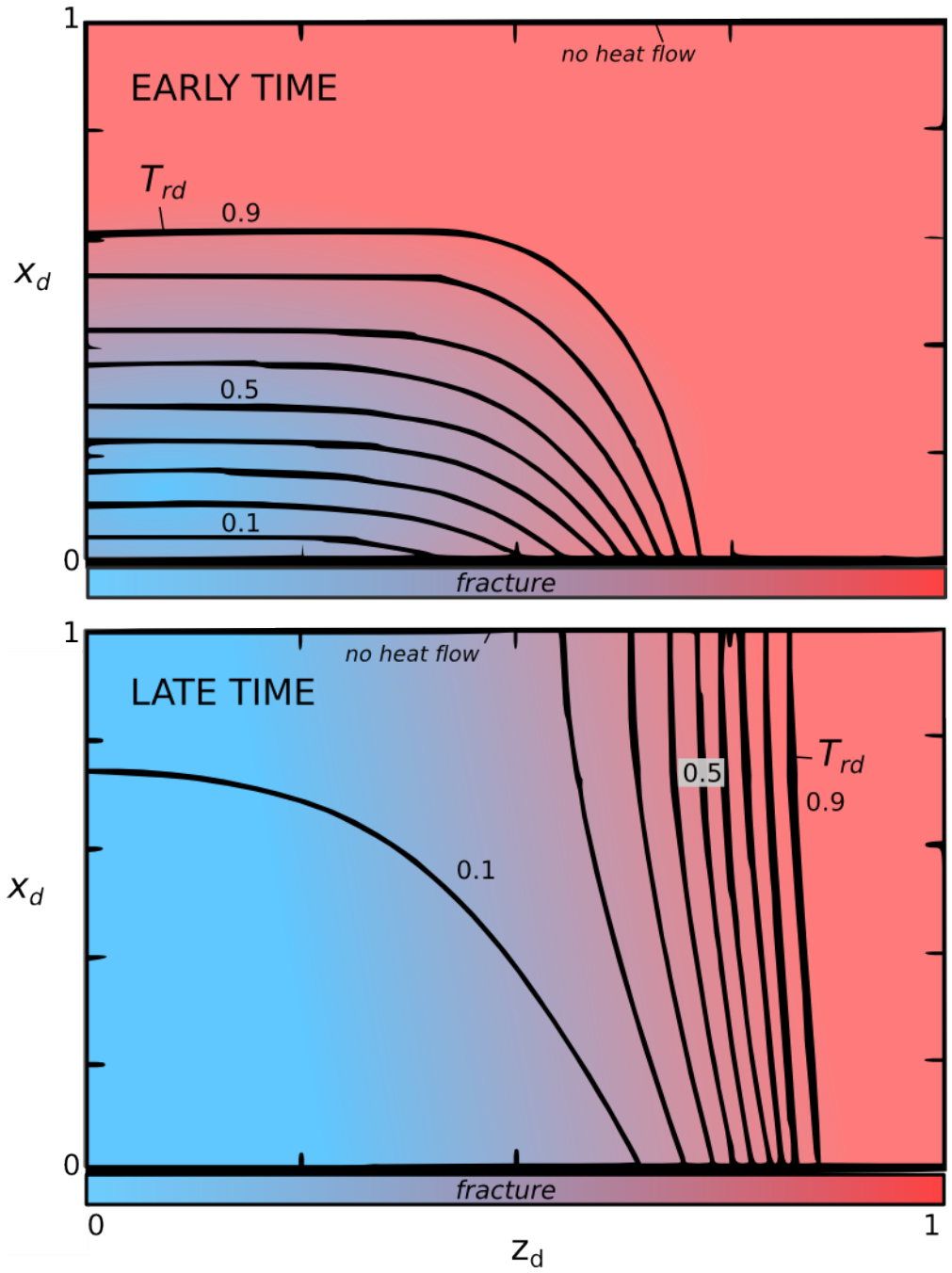

Figure 3.3: Dimensionless temperature contour distribution in the rock matrix for early and late times adapted from Bodvarsson and Tsang (1982). x_d is distance away from the fracture. The adiabatic, or no heat flow, boundary occurs at $x_d = 1$. z_d is the length along the fracture. In early times, diffusion in the rock is occurring only near the fracture. When the temperature drop (cooling front) reaches the adiabatic boundary, late-time behavior occurs and the rock matrix is depleted near the injection point. This behavior would not be known based on water outlet temperatures

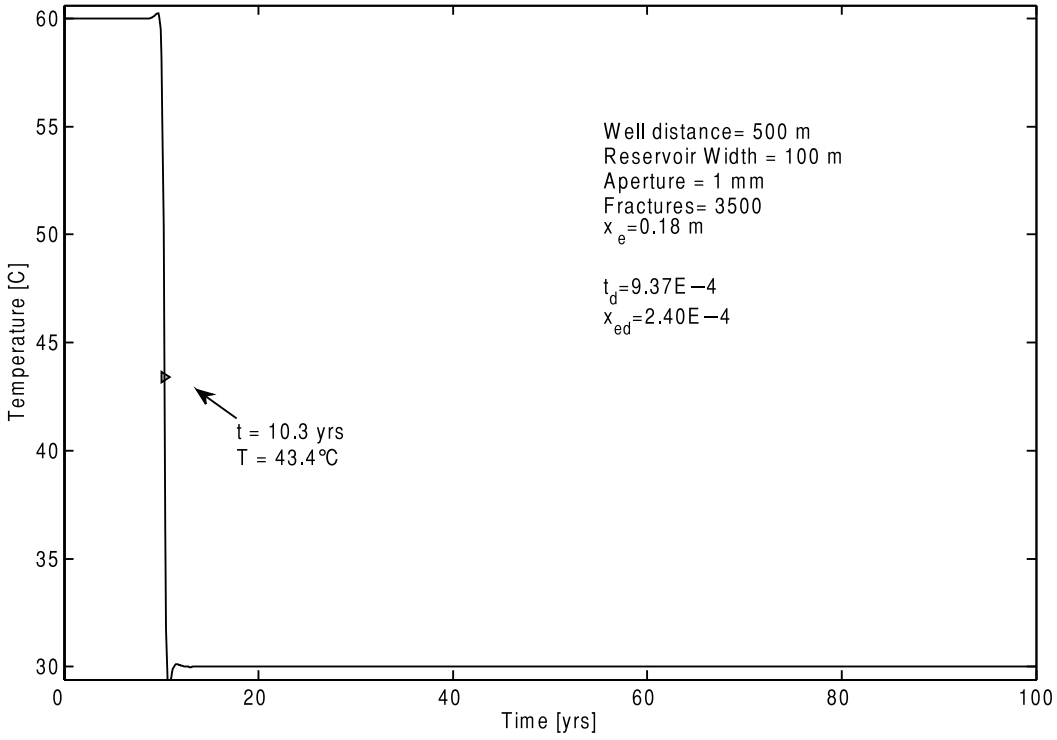

Figure 3.4: Temperature drawdown in a hypothetical highly fractured welded tuff reservoir. Small dimensionless variables indicate a rapid drop in water outlet temperatures. Within a few months, water temperatures have dropped to the temperature of injected water.

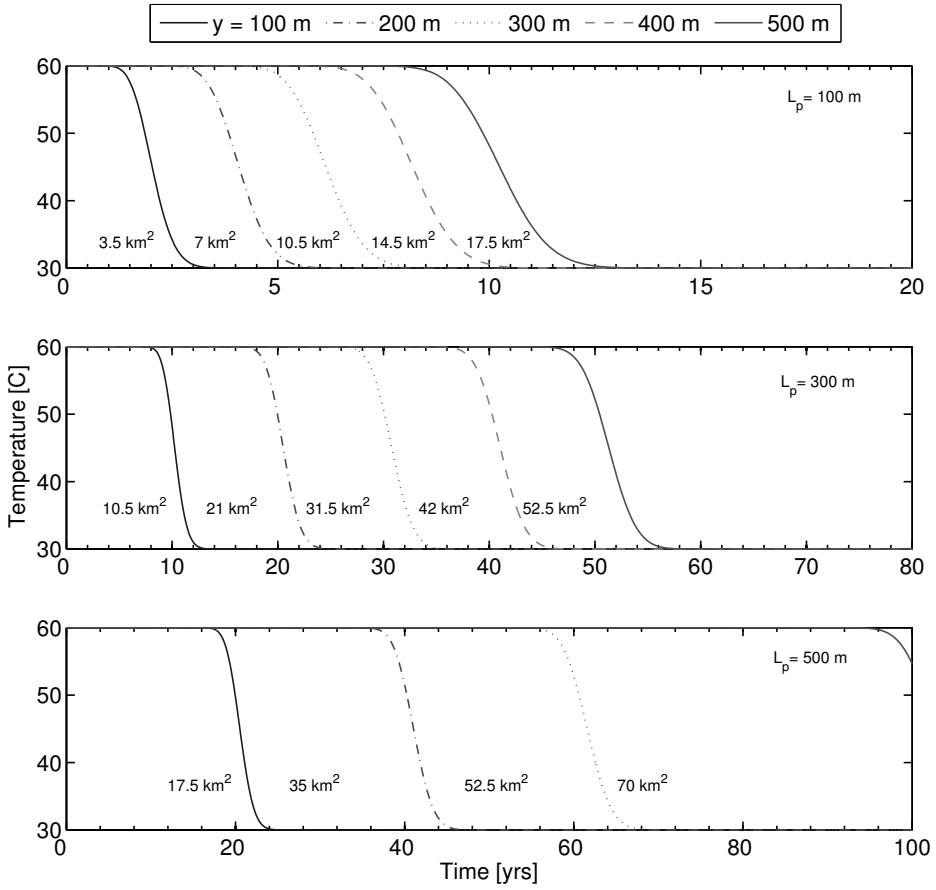

Figure 3.5: Temperature drawdown at the production well assuming 1/10th of the fractures transport fluid, effectively increasing fracture half-spacing to 1.76 m. Plots for distances between wells of 100, 300, and 500 m are shown with varying reservoir width. The areas under each curve is the total heat exchanger surface area of 350 fractures with width y and length Lp.

Table 3.1: Summary of Gringarten Model Parameters

$Q(m^3/s)$	T_{res}(°C)	T_{inj}(°C)	Aperture (mm)	x_{ed} (m)	z (m)	Fractures
0.063	60	30	1	0.176	500	3500

Chapter 4: Conclusions

The preceding chapters described various exploratory methods addressing the viability of locating a commercial EGS power plant on the Snake River Plain. Geostatistical methods document fracture spatial distribution of a core of welded tuff drilled in the central SRP. The core is one of only two 2 km deep boreholes on the SRP that access the reservoir rocks targeted for EGS development. An analytical solutions to a multi fracture heat extraction scheme shows how production and reservoir geometry parameters effect the progression of thermal drawdown in a reservoir. Though idealized, the model is beneficial in developing a development plan for use of the reservoir.

Further study of the permeability of the SRP's welded tuffs is necessary to constrain permeability in high-temperature regions. The stochastic simulations presented herein could guide target drilling depths for future exploration. The following conclusions address results of the analytical and stochastic tools in this thesis:

1. Fracture frequency indicator semivariograms have several cutoff values that suggest different controls or generating processes at discrete frequencies intervals. Extreme values for the distribution are largely gaussian, or completely random. Potential for power law distributions in these fracture frequency populations exists. Semivariogram values for cutoffs close to the mean exhibit exponential spatial correlation fairly well.

2. Dips display two domains of depth correlation. As depth increases toward the fault zone, dips steepen before becoming uniformly randomly distributed around a mean of 46°. Because there are no stress measurements, stress orientations, and fracture orientations for the borehole, we cannot accurately say what fractures are critically stressed and more likely to host fluid flow.

3. Fracture frequencies logged in the core are equivalent to the non dimensional fracture spacing,x_{ed}, of the order 10^{-1}, which corresponds to the sharp thermal front breakthrough. See figure 3.2

4. Critically stressed fractures could exist in the core if differential stress is large and are uniformly distributed with depth. EGS reservoir enhancement may take advantage of

these fractures at the simulated 150°Cand 200°Cisotherms

5. Analytical solutions accounting for multiple fractures show more efficient extraction of heat from a geothermal reservoir. The increased heat extraction rate of Gringarten's model relative to a single fracture solution demonstrates the potential to reevaluate extractable energy in existing and exploratory geothermal fields. Distributing flow amongst several fractures in the reservoir allows for lower flow rates and slower advancement of the thermal front for a given volumetric flow requirement.

6. Low aspect-ratio of distance between wells and width of fracture provide optimal heat recovery. Well arrangements that take advantage of this geometry should be explored.

7. Assumptions of uniform aperture and parallel fractures made in the Gringarten solution are not realistic. Simple applications of lognormal distributions of aperture in other studies demonstrate the hydraulic dominance of few rather than many fractures that causes single-fracture thermal behavior. While we used an arbitrary proxy of 10% of the core fractures being hydraulically conductive, no aquifer testing has been completed and bulk properties of the aquifer are still unknown.

8. Locations further east in the SRP that host higher temperature gradients in the rhyolitic tuffs may be better suited for geothermal power production. Similar geostatistical analyses and simulations would greatly benefit further geothermal exploration. With completed aquifer tests and fracture logs, INEL-1 is an ideal candidate for study.

Bibliography

Axelsson, G., Flovenz, O. G., Hauksdottir, S., Hjartarson, A., and Liu, J. (2001). Analysis of tracer test data, and injection-induced cooling, in the Laugaland geothermal field, N-Iceland. *Geothermics*, 30(6):697–725.

Barton, C. A. and Zoback, D. (1992). Self-Similar Distribution and Properties of Macroscopic Fractures at Depth in Crystalline Rock in the Cajon Pass Scientific Drill Hole. *Journal of Geophysical Research*, 97(91):5181–5200.

Barton, C. A., Zoback, M. D., and Moos, D. (1995). Fluid flow along potentially active faults in crystalline rock. *Geology*, (August):23–27.

Bertani, R. (2012). Geothermal power generation in the world 2005–2010 update report. *Geothermics*, 41(2012):1–29.

Blackwell, D. and Richards, M. (2004). Geothermal Map of North America.

Blackwell, D., Stepp, P., and Richards, M. (2010). Comparison and Discussion of the 6 Km Temperature Maps of the Western US Prepared by the SMU Geothermal Lab and the USGS. In *GRC Transactions*, pages 515–520.

Blackwell, D. D. (1989). Regional implications of heat flow of the Snake River Plain, Northwestern United States. *Tectonophysics*, 164(2–4):323–343.

Bodvarsson, G. and Tsang, C.-f. (1982). Injection and Thermal Breakthrough in Fractured Geothermal Reservoirs. *Journal of Geophysical Research*, 87(B2):1031–1048.

Branney, M. J., Bonnichsen, B., Andrews, G. D. M., Ellis, B., Barry, T. L., and McCurry, M. (2007). 'Snake River (SR)-type' volcanism at the Yellowstone hotspot track: distinctive products from unusual, high-temperature silicic super-eruptions. *Bulletin of Volcanology*, 70(3):293–314.

Brott, A., Blackwell, D. D., and Ziagos, J. P. (1981). Thermal and Tectonic Implications of Heat Flow in the Eastern Snake River Plain. *Journal of Geophysical Research*, 86(B12):11,709–11,734.

Byerlee, J. (1978). Friction of Rocks. *Pure and applied Geophysics*, 116:615–626.

Carena, S., Suppe, J., and Kao., H. (2002). Active detachment of Taiwan illuminated by small earthquakes and its control of first-order topography. *Geology*, 30(10):935–938.

Carmona, E., Almendros, J., Peña, J., and Ibáñez, J. (2010). Characterization of fracture systems using precise array locations of earthquake multiplets: An example at Deception Island volcano, Antarctica. *Journal of Geophysical Research: Solid Earth*, 115(B6):1978–2012.

Carslaw, H. and Jaeger, J. (1959). *Conduction of heat in solids.pdf*. Oxford University Press, London, 2nd editio edition.

Christiansen, E. (2014). Lithologic log of the kimberly borehole. Working figure.

Cole, J., Milner, D., and Spinks, K. (2005). Calderas and caldera structures: a review. *Earth-Science Reviews*, 69(1-2):1–26.

de Hoog, F., Knight, J. H., and Stokes, A. (1982). An improved method for numerical inversion of Laplace transforms. *J. Sci. and Stat. Comput.*, 3(3):357–366.

DeNosaquo, K. R., Smith, R. B., and Lowry, A. R. (2009). Density and lithospheric strength models of the Yellowstone–Snake River Plain volcanic system from gravity and heat flow data. *Journal of Volcanology and Geothermal Research*, 188(1-3):108–127.

Deutsch, C. V. (2002). *Geostatistical Reservoir Modeling*. Oxford University Press.

Deutsch, C. V. and Journel, A. G. (1998). *GSLIB: Geostatistical Library and User's Guide*. Oxford University Press, New York.

Doe, T., Mclaren, R., and Dershowitz, W. (2014). Discrete Fracture Network Simulations of Enhanced Geothermal Systems. In *Proceedings, 39th Workshop on Geothermal Reservoir Engineering*, pages 1–11, Palo Alto, CA.

Doherty, D., McBroome, L., and Kuntz, M. (1979). Preliminary geological interpretation and lithologic log of the exploratory geothermal test well (INEL-1). Technical report, USGS.

Donaldson, I. G. (1982). Heat and mass circulation in geothermal systems. *Ann. Rev. Earth Planetary Science*, (1975):377–395.

Embree, G. F., Phillips, W. M., Champion, D., Moore, D. K., Jordan, B. R., and Geissman, J. W. (2011). Large-Scale Rheomorphic Structures and Basalt Stratigraphy of the Newdale and Linderman Dam 7 . 5-minute Quadrangles , Eastern Snake River Plain , Idaho. In *GSA Annual Meeting*, number 2008.

Engdahl, E. and Villaseñor, A. (2002). Global Seismicity: 1900–1999. In Lee, W., Kanamori, H., Jennings, P., and Kisslinger, C., editors, *International Handbook of Earthquake and Engineering Seismology*, pages 665–690. Academic Press.

Faulds, J. E., Hinz, N., Kreemer, C., and Coolbaugh, M. (2012). Regional Patterns of Geothermal Activity in the Great Basin Region , Western USA : Correlation With Strain Rates Distribution of Geothermal Fields. *GRC Transactions*, 36:897–902.

Faybishenko, B. and Benson, S. (2000). Preface. In Faybishenko B, Witherspoon PA, B. S., editor, *Dynamics of fluids in fractured rock*, page ix. American Geophysical Union, Washington, D.C.

Fuller, C. M. and Sharp, J. M. (1992). Geological Society of America Bulletin Permeability and fracture patterns in extrusive volcanic rocks : Implications from the welded Santana Tuff , Trans-Pecos Texas Permeability and fracture patterns in extrusive volcanic rocks : Implications from the we. *Geological Society of America Bulletin*, 104(November):1485–1496.

Geissman, J. W., Holm, D., Harlan, S. S., and Embree, G. F. (2010). Rapid, high-temperature formation of large-scale rheomorphic structures in the 2.06 Ma Huckleberry Ridge Tuff, Idaho, USA. *Geology*, 38(3):263–266.

Goovaerts, P. (1997). *Geostatistics for Natural Resources Evaluation*. Oxford University Press, New York.

Gringarten, A., Witherspoon, P., and Ohnishi, Y. (1975). Theory of Heat Extraction from Fractured Hot Dry Rock. *Journal of Geophysical Research*, 80(8):1120–1124.

Hickman, S. H. and Zoback., M. D. (1983). The interpretation of hydraulic fracturing pressure-time data for in situ stress determination. In *Hydraulic Fracturing Measurements*, pages 44–54.

Hudson, J. A. and Priest, S. (1983). Discontinuity frequency in rock masses. *J. Rock Mech. Min. Sci. Geomech.*, 20:73–89.

Isaaks, E. H. and Srivastava, R. M. (1989). *An introduction to applied geostatistics*. Oxford University Press, New York.

Kolstad, C. and McGetchin, T. (1978). Thermal Evolution Models for the Valles Caldera with reference to a hot dry rock geothermal experiment. *Journal of Volcanology and Geothermal Research*, 3:197–218.

Kuntz, M. A., Covington, H. R., and Schorr, L. J. (1992). An overview of basaltic volcanism of the eastern Snake River Plain, Idaho. In *Geological Society of America Memoirs, 179*, pages 227–268. Chicago.

LeCain, G. D. (1997). Air-Injection Testing in Vertical Boreholes in Welded and Nonwelded Tuff , Yucca Mountain , Nevada. Technical report, U.S. Geological Survey.

LeCain, G. D. and Stuckless, J. S. (2012). Hydrology of the unsaturated zone, Yucca Mountain, Nevada. In *Geological Society of America Memoirs, 209*, pages 9–72.

Leeman, W. (1982). Development of the Snake River Plain-Yellowstone Plateau Province , Idaho and Wyoming : An Overview and Petrologic Model. In Bonnichsen, B. and Breckenridge, R., editors, *Cenozoic Geology of Idaho*, pages 155–177. Idaho Bureau of Mines and Geology.

Manning, C. and Ingebritsen, S. (1999). Permeability of the continental crust: Implications of geothermal data and metamorphic analysis. *Reviews of Geophysics*, 37:127–150.

Millard, M. A., Clayton, R. W., and Painter, C. S. (2005). Preferred fracture orientations resulting from secondary deformation of a rhyolitic ash flow tuff: 2 Ma Huckleberry Ridge Tuff, Southeast Idaho. In *GSA Annual Meeting*, number 89, page 91954, Salt Lake City.

Moos, D. and Barton, C. A. (1990). In-situ stress and natural fracturing at the INEL site, Idaho. Technical report.

Morgan, L. A., Doherty, D. J., and Leeman, W. P. (1984). Tuff of Blue Creek Elkhorn c , f Tuff of Blacktail. *Journal of Geophysical Research*, 89(B10):8665–8678.

Morgan, L. A. and McIntosh, W. C. (2005). Timing and development of the Heise volcanic field, Snake River Plain, Idaho, western USA. *Geological Society of America Bulletin*, 117(3):288.

Neuman, S. P. (2005). Trends, prospects and challenges in quantifying flow and transport through fractured rocks. *Hydrogeology Journal*, 13(1):124–147.

Payne, S., McCaffrey, R., King, R., and Kattenhorn, S. (2012). A new interpretation of deformation rates in the Snake River Plain and adjacent basin and range regions based on GPS measurements. *Geophysical Journal International*, 189(1):101–122.

Pierce, K. L. and Morgan, L. A. (1992). The track of the Yellowstone hotspot: Volanism, faulting, and uplift. In Link, P., Kuntz, M., and Platt, L., editors, *Regional Geology of Eastern Idaho and Western Wyoming: GSA Memoir 179*, pages 1–53.

Pollyea, R. M. and Fairley, J. P. (2012). Implications of spatial reservoir uncertainty for CO2 sequestration in the east Snake River Plain, Idaho (USA). *Hydrogeology Journal*, 20(4):689–699.

Puskas, C. M., Smith, R. B., Meertens, C. M., and Chang, W. L. (2007). Crustal deformation of the Yellowstone–Snake River Plain volcano-tectonic system: Campaign and continuous GPS observations, 1987–2004. *Journal of Geophysical Research*, 112(B3):B03401.

Pytharouli, S. I., Lunn, R. J., Shipton, Z. K., Kirkpatrick, J. D., and do Nascimento, A. F. (2011). Microseismicity illuminates open fractures in the shallow crust. *Geophysical Research Letters*, 38(2).

Rao, A., Chen, Y.-C., Lee, S., Leigh, J., Johnson, A., and Renambot, L. (2005). Corelyzer: Scalable Geologic Core Visualization using OSX, Java and OpenGL.

Self, S., Goff, G., Gardner, J., Wright, J., and Kite, W. (1986). Explosive rhyolitic volcanism in the Jemez Mountains: vent locations, caldera development and relation to regional structure. *Journal of Geophysical Research*, 91(B):1779–1798.

Shervais, J. W. (2014). Personal Communication.

Shervais, J. W., Kauffman, J. D., Gillerman, V. S., Othberg, K. L., Vetter, S. K., Hobson, V. R., Cooke, M. F., Matthews, S. H., and Hanan, B. B. (2005). Basaltic volcanism of the central and western Snake River Plain : A guide to fi eld relations between Twin Falls and Mountain Home , Idaho.

Shervais, J. W., Schmitt, D. R., Nielson, D., Evans, J. P., Christiansen, E. H., Morgan, L., Shanks, W. C. P., Prokopenko, A. a., Lachmar, T., Liberty, L. M., Blackwell, D. D., Glen, J. M., Champion, D., Potter, K. E., and Kessler, J. a. (2013). First Results from HOTSPOT: The Snake River Plain Scientific Drilling Project. *Scientific Drilling*, (15, March 2013):36–45.

Shervais, J. W., Vetter, S. K., and Hanan, B. B. (2006). Layered mafic sill complex beneath the eastern Snake River Plain: Evidence from cyclic geochemical variations in basalt. *Geology*, 34(5):365.

Smith, R. P. (2004). Geologic Setting of the Snake River Plain Aquifer and Vadose Zone. *Vadose Zone Journal*, 3(1):47–58.

Smyth, R. C. and John M. Sharp, J. (2006). The hydrology of tuffs. In Heiken, G., editor, *Tuffs: Their properties, uses, hydrology, and resources*, chapter 4.1, pages 91–111. GSA.

Stock, J. M., Healy, J. H., Hickman, S. H., and Zoback, M. D. (1985). Hydraulic fracturing stress measurements at Yucca Mountain, Nevada, and relationship to the regional stress field. *Journal of Geophysical Research*, 90(B10):8691.

Terzaghi, R. (1965). Sources of error in joint surveys. *Geotechnique*, (15):287–304.

Tester, J. W., Anderson, B. J., Batchelor, A. S., Blackwell, D. D., DiPippo, R., Drake, E. M., Garnish, J., Livesay, B., Moore, M. C., Nichols, K., Petty, S., Toksoz, M. N., and Veatch, R. W. J. (2006). The Future of Geothermal Energy: Impact of Enhanced Geothermal Systems on the United States in the 21st Century. Technical Report November, Massachusetts Institute of Technology and Department of Energy.

Welhan, J. A. and Reed, M. F. (1997). Geostatistical analysis of regional hydraulic conductivity variations in the Snake River Plain aquifer , eastern Idaho. *Geological Society of America Bulletin*, 109(7):855–868.

Wohletz, K. and Heiken, G. (1992). *Volcanology and Geothermal Energy*. Uniersity of California Press.

Zoback, M. L. and Zoback, M. (1980). State of Stress in the Conterminous United States. *Journal of Geophysical Research*, 85(No. B11):6113–6156.

Appendix

Temperature of water in fracture

$$b\rho_w c_w \left[\frac{\partial T_w(z,t)}{\partial t} + v\frac{\partial T_w(z,t)}{\partial z}\right] = \frac{\partial^2 T_r(x,z,t)}{\partial x^2}|_{x=b}$$

Heat diffusion through the rock

$$\frac{\partial^2 T_R(x,z,t)}{\partial x^2} = \frac{\rho_R c_R}{K_R}\frac{\partial T_R(x,z,t)}{\partial t}$$

Initial and Boundary Conditions

$$T_r(x,z,t) = T_w(z,t) = T_{ro} - \omega z \qquad \frac{z}{v}$$

$$T_r(x,0,t) = T_w(0,t) = T_{ro} \qquad t < 0$$

$$T_r(x,0,t) = T_w(0,t) = T_{wo} \qquad t \geq 0$$

$$T_w(z,t) = T_r(b,z,t) \qquad \forall \quad z,t$$

$$\frac{\partial T_R(x,z,t)}{\partial x}|_{x=x_E} = 0$$